VECC/EXP/QGP/97-04
STARNOTE∆#310∆Oct. 1997

PHOTON MULTIPLICITY MEASUREMENTS IN THE STAR DETECTOR AT RHIC

A Proposal for Upgrade of STAR[1]

Bhubaneswar - Calcutta - Chandigarh - Jaipur - Jammu - Mumbai

[1]in continuation of the proposal submitted in July 1994 and in October 1996.

List of Collaborators[2]

Institute of Physics, Bhubaneswar
D.P. Mahapatra, S.C. Phatak

Variable Energy Cyclotron Centre, Calcutta
S. Chattopadhyay, M.R. Dutta Mazumdar, Murthy S. Ganti, T.K. Nayak, S. Ramanarain, Bikash Sinha, M.D. Trivedi, Y.P. Viyogi[3]

Panjab University, Chandigarh
M.M. Aggarwal, V.S. Bhatia

University of Rajasthan, Jaipur
K.B. Bhalla, V. Kumar, R. Raniwala, S. Raniwala

University of Jammu, Jammu
P.V.K.S. Baba, S.K. Badyal, N.K. Rao, S.S. Sambyal

Indian Institute of Technology, Mumbai
R. Varma

[2]Only permanent members are listed. In addition there are several graduate students.
[3]Contact-person

Address for correspondence :
Variable Energy Cyclotron Centre
Bidhan Nagar, Calcutta 700064 (INDIA)

(tel: 91 33 3371230, fax : 91 33 3346871)
e-mail : viyogi@vecdec.veccal.ernet.in

Abstract

It is proposed to integrate the WA98 preshower Photon Multiplicity Detector (PMD) with some modifications into the STAR experiment to study photon production and isospin fluctuations in nucleus-nucleus collisions at RHIC energy in order to investigate the formation of Quark-Gluon Plasma (QGP), the dynamics of hadronization process, the characteristics of the hot hadron gas and to search for Disoriented Chiral Condensates (DCCs). The PMD, to be mounted at 7 m from vertex, will have fine granularity and almost full azimuthal coverage in the pseudo-rapidity region $2.0 \leq \eta \leq 3.8$. Simulation results are presented to describe the effectiveness of the proposed detector to measure photon multiplicity on event–by–event basis in the actual environment of the STAR experiment. Background problems caused by material in front of the PMD are also investigated and the efforts to reduce the background by implementing a charged particle veto are described. Coupled with the Forward TPC measuring charged particles, the PMD should become an ideal tool to search for any physical processes leading to charge–neutral fluctuations. In the given environment one can achieve photon counting efficiency of better than 65% and the associated background from all sources amount to less than 35%. The event-to-event fluctuation of the measured N_γ/N_{ch} ratio will be better than 10%. We show that the PMD can provide reasonable selection on low p_T photons suitable for DCC searches and also estimates of global transverse electromagnetic energy.

Contents

1 Specialised Physics Issues

The basic aim of adding a photon multiplicity detector (PMD) system in STAR is to study photon production and isospin fluctuations in nucleus-nucleus collisions at RHIC energy in order to investigate the formation of Quark-Gluon Plasma (QGP), the dynamics of hadronization process, the characteristics of the hot hadron gas and to search for Disoriented Chiral Condensates (DCCs). In conjunction with the measurement of charged particles in the Forward TPC the PMD will greatly enhance the physics capabilities in the areas described below.

1.1 Isospin Fluctuations and the DCC

Several theoretical studies [1, 2, 3, 4, 5, 6, 7, 8] have suggested that the chiral phase transition may occur at high temperature (T > T_c) in ultra-relativistic hadronic and nuclear collisions. In this case a piece of strong interaction vacuum may be produced with unconventional orientation of the chiral order parameter. This domain of Disoriented Chiral Condensate (DCC) is then supposed to decay into coherent semi-classical pion field having the same chiral orientation. One of the consequences of the eventual decay of the DCC domain, as it cools below T_C, is the large imbalance in the emission of neutral to charged pions given by the probability[1, 2]:

$$P(f) = \frac{1}{2\sqrt{f}} \tag{1}$$

$$\text{where} \quad f = \frac{N_{\pi^0}}{N_{\pi^0} + N_{\pi^+} + N_{\pi^-}} \sim \frac{N_\gamma/2}{N_\gamma/2 + N_{\rm ch}}. \tag{2}$$

N_γ and $N_{\rm ch}$ are multiplicities for photons and charged particles, respectively. This assumes all charged particles are pions and all photons come from π^0 decay. The generic distribution from normal events will be binomial with peak at f $\approx$ 1/3. Large isospin fluctuations have also been predicted [9] in other scenarios of the hadronization process of quark gluon plasma. Exotic events having such large isospin fluctuations have already been observed in cosmic ray experiments [10, 11]. Recently there has been further upsurge in the searches for these exotics in accelerator-based experiments both in pp [12] and in heavy ion studies[13, 14].

A precision measurement of N_γ to $N_{\rm ch}$ distributions over a large phase space provides a unique tool for the search of disoriented chiral condensates.

Although there is no clear guidance about the region of phase space where one should look for the DCC, there have been suggestions [1, 15] that these exotic effects might be better studied at larger rapidities. The pions emitted from the DCC domains are predicted to have low p_T, usually smaller than 200 MeV/c. Measuring photons with such low p_T in the mid-rapidity regions is difficult as the energies are low and hence photon detection efficiencies are also lower. But at larger rapidities these photons appear with large momenta and measurements become easier. This advantage is one of the main reasons to implement the PMD in the forward rapidity regions.

The PMD–FTPC pair in the STAR experiment should enable us to study in detail the formation of the DCC in about two units of pseudo-rapidity in the forward region.

1.2 Global Observables, Fluctuations and Event Shapes

Multiplicity fluctuations are a signature for the critical phenomena at the onset of phase transition. Plasma instabilities causing directional flow of particles localised in rapidity can be detected by the analysis of azimuthal event–by–event fluctuations. The internal inhomogeneity of the system created in central nucleus-nucleus collisions can be studied by the event–by–event analysis of the fluctuations of the summed variable [16]

$$Z = \sum_{i=1}^{N} z_i \tag{3}$$

where $z = x_i - \langle x \rangle$, x_i is any single particle kinematic variable such as rapidity and the sum runs over all the detected particles. The method requires a detailed comparison of nucleon-nucleon and nucleus-nucleus interactions.

The PMD with its ability to measure $N_\gamma(\eta, \phi)$ with fine granularity over almost two units of pseudo-rapidity and with full azimuthal coverage is best suited to study the event fluctuations mentioned above. In addition the ratio N_γ/N_{ch} can be used as a off-line trigger to indicate the presence of photon excess/depletion over normal events, with which one can look for related effects in other observables of the event. The estimation of transverse e.m. energy E_T^{em} should also provide opportunities for the study of fluctuations in other kinematic variables.

The PMD can be used to study the event shapes and investigate the occurrence of rapidity gaps and other fluctuations in spatial distribution of photons because of its fine granularity and moderately large coverage. The photon distributions measured by the WA93 PMD have been successfully utilised to study the azimuthal anisotropy, a consequence of directed flow [17]. Selection of non-statistical fluctuations will be another important study [18]. The STAR experiment will have a very comprehensive programme of event–by–event fluctuation studies [19] and the PMD should also add to the capabilities.

1.3 Direct Photon Production

Production of direct thermal photons is one of the most interesting signatures of QGP formation. Measurement of N_γ/N_{ch} can also be used to study the production of direct photons in the reaction. Multiplicity dependence of the photon yield is expected to be quite different for direct photons and conventional sources and this may provide a more sensitive tool to disentangle the direct photon contribution. For the decay photons N_γ varies linearly with $dN_{ch}/d\eta$, but for the directly produced photons, N_γ will vary as $(dN_{ch}/d\eta)^x$, where $x \approx 1.2$ [20].

The photon yield G measured as a function of charged particle rapidity distribution can be written, under suitable normalisation, as [21] :

$$G(dN_{ch}/d\eta) = C[1 + \alpha.(dN_{ch}/d\eta)^{x-1}] \tag{4}$$

where α is a measure of the first order deviation from linearity and C is a suitable normalisation factor. Non-zero values of α, which are statistically significant, should indicate the presence of unusual phenomena associated with the production of direct photons. This will be possible by measuring the pseudo-rapidity distributions of charged particles and photons with good accuracy in the same part of the phase space.

2 Photon Multiplicity Detector System

The preshower photon multiplicity detector has already been implemented in the WA93 and WA98 experiments at the CERN SPS [22, 23]. The photon multiplicity detector system for STAR consists of two subsystems: (a) the preshower detector with converter referred to as the PMD and (b) the charged particle veto (CPV).

The salient parameters of the proposed subsystem in STAR are given in Table I. The CPV will be used to reject the charged particles giving signal in the preshower part to reduce the background from hadronic secondaries.

TABLE I
Geometrical Characteristics of the PMD System in STAR

	CPV	**PMD**
Distance from the vertex	6.97 m	7 m
Pseudo-rapidity Coverage	2.0−3.75	2.0−3.75
Active area	13.5 m^2	13.5 m^2
Detector Technology	Cellular gas PC	Scint. pads
Total number of channels	45600	45600

2.1 Photon Counting : Basic Concepts

Photon multiplicity measurements on an event–by–event basis become viable and useful when the number of photons falling on the detector is substantial to result in smaller fluctuation in the measured N_γ distributions. For the STAR PMD acceptance this number will be of the order of 900 in central Au + Au collisions, having event-to-event fluctuation of less than 5%. It should then be possible to measure N_γ on an event–by–event basis to distinguish events having N_γ/N_{ch} values substantially different from normal events.

The principle of operation of a preshower PMD can be found in detail in Ref. [25]. The detector basically consists of a finely segmented plane of sensitive material (plastic scintillators in the case of WA93/WA98, and also to be implemented in STAR) behind a suitable converter (3 X_0 thick lead plates). The converter thickness is selected for maximising the conversion efficiency and minimising the shower overlap and the effect of secondaries arising due to hadronic interactions in the converter. The principle of photon identification in the PMD makes use of the fact that photons are much more likely to shower in the lead converter and produce a large signal in the sensitive medium, while non-showering hadrons will produce a signal corresponding to single minimum ionising particle (MIP). For counting of photons, fired pads are clustered and the total signal and the centroid position of the clusters determined for the event. Hadrons are rejected either by applying a threshold on the preshower signal or by other suitably selected criteria. The remaining clusters are called γ-like. This has some admixture of clusters arising due to hadronic interactions in the converter which remain even after the application of hadron rejection criteria. This admixture constitutes background in photon counting.

The number of incident photons N_γ is obtained from the measured number of γ-like clusters $N_{\gamma-like}$ using the prescription :

$$N_\gamma = (N_{\gamma-like} - N_\gamma^b)/\epsilon_\gamma \tag{5}$$

where N_γ^b is the number of background clusters in the $N_{\gamma-like}$ sample and ϵ_γ is the *photon counting efficiency.* The photon counting efficiency ϵ_γ is defined as the ratio of the number of photon clusters identified after vetoing and the total number of incident photons. This is determined by detailed simulation and test beam measurements of the detector characteristics.

The photon counting efficiency ϵ_γ depends on several factors, e.g., the conversion probability, the hadron rejection criteria applied, the granularity and the associated clustering efficiency. The photon counting efficiency also depends on centrality and pseudo-rapidity because of the changing particle multiplicity and the energy of photons. The roles of all these factors have been investigated in detail for the WA93 and WA98 PMDs [26, 24].

For generic events the background arising due to hadronic interactions can be obtained from detailed simulation. About 15% of the incident hadrons interact in the 3 X_0 thick lead converter. It is useful to express the background N_γ^b as a fraction of the total number of γ-like clusters as :

$$N_\gamma^b = f_{bkg} \times N_{\gamma-like} \tag{6}$$

the quantity f_{bkg} being called the *background fraction.* The fraction of background clusters which appears as γ-like after the application of hadron rejection criteria may vary from 10% to 40% depending on the efficiency of the criteria applied and the multiplicity environment. In the case of WA93/WA98 PMD, f_{bkg} was found to be $\sim$ 30–35% after applying 3 MIP threshold on the cluster signal to reject hadrons.

However in a situation where the event may have large charge-to-neutral fluctuations, this estimation may not be proper. It is desired to have measurements of charged particle multiplicity in the same part of the phase space on event–by–event basis to estimate the background to be used in Eqn. 5 above. This has been attempted in the WA98 experiment using the data from charged particle multiplicity detectors. If the charged particle detector is located at some distance from the PMD and there are intervening materials, then the number of hadrons falling on the PMD may differ because of multiple scattering. Photons may also get converted in the upstream materials and produce more than one cluster at the PMD. It is therefore necessary to implement a charged particle veto in close proximity of the PMD to handle both the charged particle background and also upstream conversion of photons.

2.2 Photon Multiplicity Detector

2.2.1 Mechanical Description

The PMD in STAR will be a modified version of the one used in the WA98 experiment [24] which is very similar to that used in the WA93 experiment and described in detail in Ref. [25]. It consists of a matrix of small plastic scintillator pads placed behind $3X_0$ thick lead converter plate and held on an iron stand. The light from the scintillator pads is collected and transported to the readout device by wavelength shifting (WLS) plastic optical fibres. To improve light transport, short lengths of the WLS fibres are used and these are spliced to longer length clear plastic fibres. The pads are either painted using reflector paint or wrapped in aluminized mylar foil to improve the light collection and to eliminate cross-talk.

A set of 50×38 pads are enclosed in a matrix form in one light tight box module. The fibre ends of these 1900 pads are inserted into a perforated plate having 50×38 closely spaced holes in a matrix form, maintaining the correspondence between the pad coordinates in the box and the fibre coordinates in the perforated plate. About 5% of these pads, randomly selected over the matrix, have another fibre inserted to launch light in these selected pads from an externally triggered LED. These 'fiducial' pads are used to generate the correspondence between the physical fibre space and the pixel space of the readout device (the pixel-to-fibre maps).

The PMD for STAR will consist of 12 box modules of 15 mm pads from the WA98 experiment and 12 box modules of 12 mm pads which will be freshly fabricated. Lead converter will be the same as in WA98 with 3 X_0 thickness. It will be mounted at a distance of 7 meters from the vertex. Such a large distance from the vertex is required to handle the multiplicity. The proposed layout of the PMD box modules for STAR is shown in Fig. 1. The new boxes will also have a matrix of 50 $\times$ 38 pads with WLS fibres. The central hole will accommodate the vertex position detector (VPD). The $(\eta - \phi)$ – coverage for the PMD placed at 7 m from vertex is shown in Fig. 2. For the major part, the ϕ-coverage is full. This will greatly help in the study of event shapes and fluctuations.

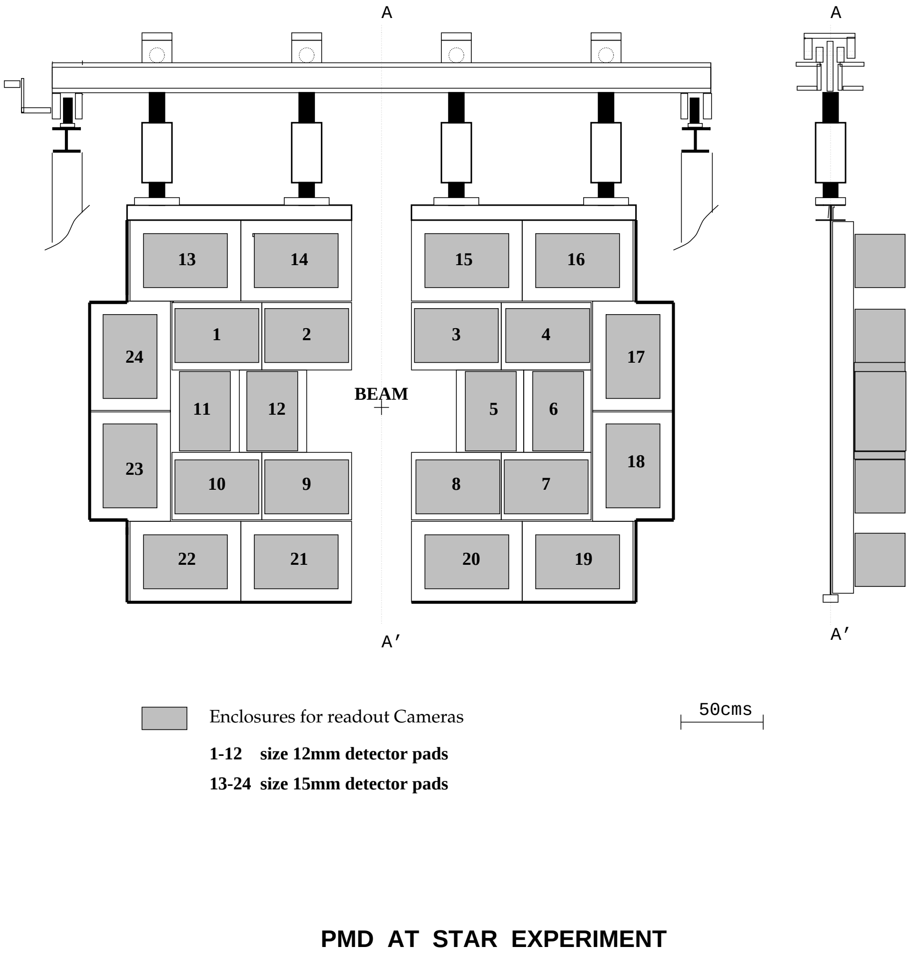

Figure 1: Layout of the box modules in STAR PMD. The inner hole is 30 cms $\times$ 29 cms. The distance from vertex is 7 m.

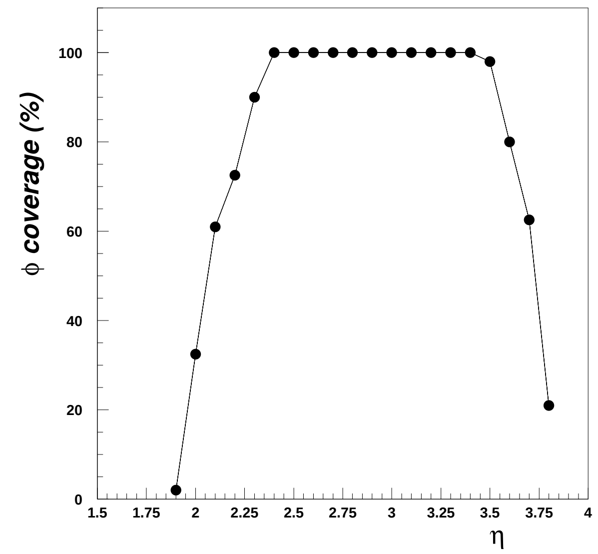

Figure 2: $\eta - \phi$ coverage of the STAR PMD.

2.2.2 Electronics and Readout

The bundle of 1900 fibres in each box module is read out using one Image Intensifier(II) + CCD readout system obtained from the UA2 experiment [27]. A light gain of about 40000 is obtained in the three stages of the II chain equipped with a micro-channel plate in the second stage. The CCD pixel charge is digitized using a custom-built fastbus module employing 8-bit 20 MHz FADC obtained from the UA2 group. The pixel-to-fibre map can be loaded into the digitizer and a compact data format containing the fibre number, the sum of the contributions from all the pixels assigned to that fibre and the total number of contributing pixels can be generated by the fastbus module. Data can be recorded either in the form of pixel signals or in the form of compressed fibre signals or in a composite format. Recording of data in fiber format reduces the data volume drastically thereby reducing the PMD readout dead time.

MCP voltages are kept always ON during data taking until some trigger arrives. After the arrival of the event trigger, II gate is applied to make the system blind to further incident particles. This gating can be applied within 100 ns of the arrival of trigger. This reduces the possibility of recording pile-up events occuring after the arrival of real trigger.

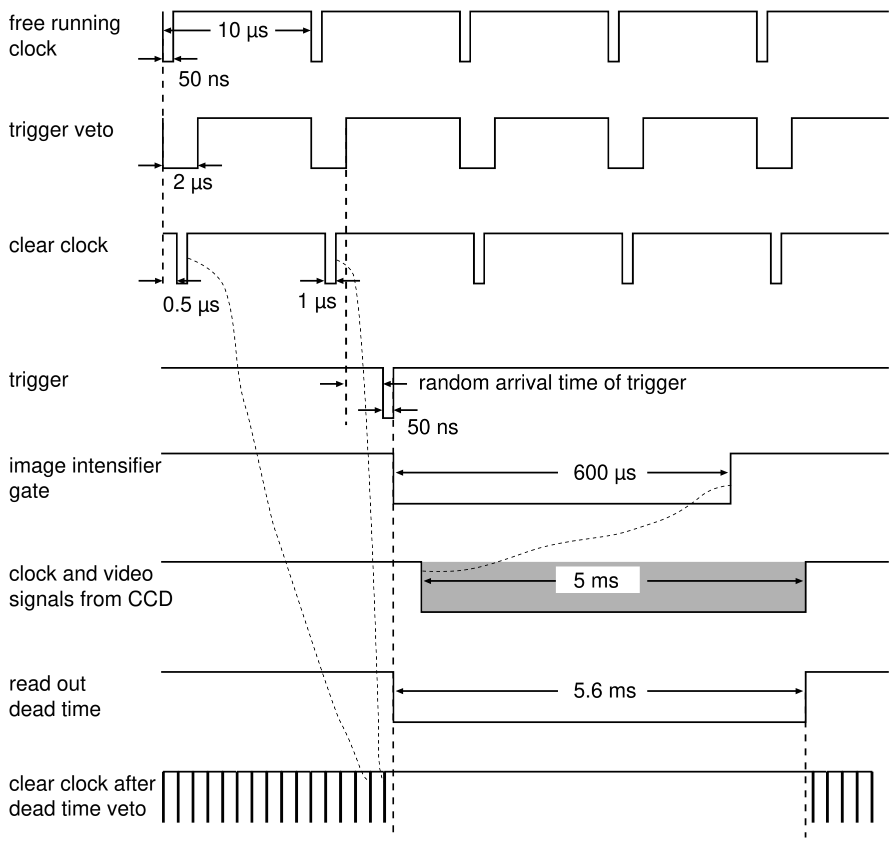

Figure 3: Timing Diagram for the CCD Readout.

The timing sequences used for the readout of the camera is shown in Fig. 3. A 1 μs wide pulse is generated every 10 μs to the CCD electronics for clearing the CCD. Fast clearing of the CCD within 1 μs is achieved with the use of antiblooming electrodes. The gates which are generated along with the arrival of the trigger pulse are (a) 600 μs and (b) 5.6 ms. The 600 μs wide pulse is used to generate the gate of 430 V which blocks the transfer of electrons through one of the stages of the image intensifier during the period when the transfer of pixel data from the image zone to the memory zone of the CCD takes place. Total readout time taken for the whole frame of the CCD is 5.6 ms. The timing logic also ensures that no trigger arrives during the readout. The clear clock is vetoed with 5.6 ms wide pulse for the arrival of a trigger until the readout is finished. The efficiency of clearing the camera by each clear pulse is 99.5%.

2.3 Charge Particle Veto

2.3.1 Mechanical Description

The design of the CPV detector should satisfy, ideally, the requirements of high granularity, good rate capability, low cross-talk between adjacent channels and high efficiency. We have designed thin gas cellular proportional chambers with honeycomb cells and wire readout to be configured as CPV. The design reduces neighbouring channel cross-talk resulting from signals induced by δ-electrons [28] and eliminates the need of pickup pads thus lowering the input capacitance.

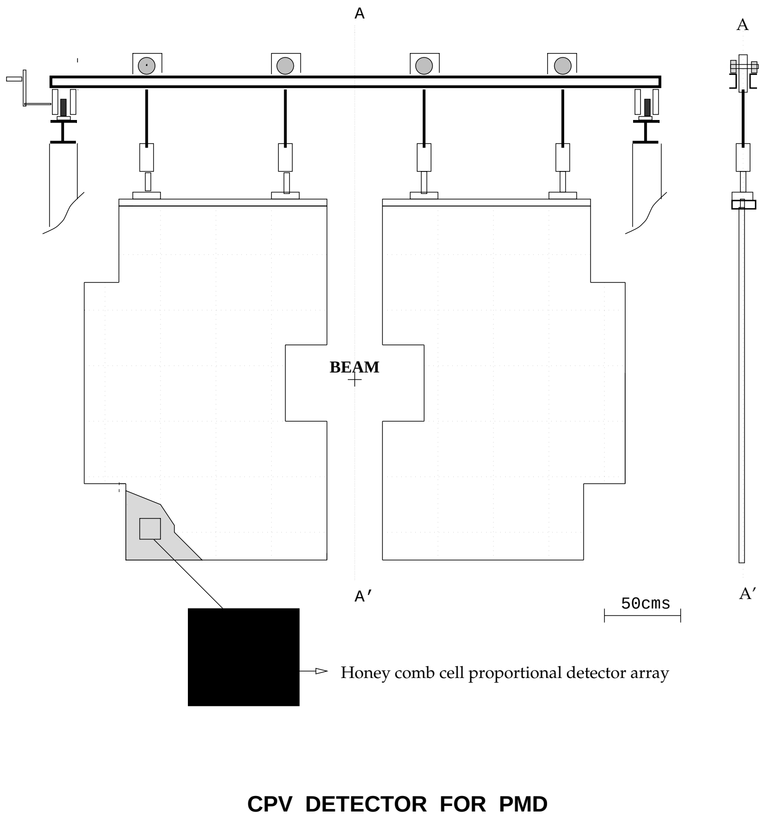

Figure 4: Layout of the STAR CPV.

The mechanical part of the detector consists of a thin (8 mm) gas volume enclosed between two G10 boards and divided into regular honeycomb cells by thin moulded plastic separator walls. These walls are metallized and graphite coated to reduce photoelectron emission and form a common cathode for all the cells. The cells have area comparable to that of the pads of the PMD. Gold plated tungsten wires of 20 μm dia. are stretched (with 30–35 gm tension) between the G10 boards, pass through the centres of the hexagonal cells and act like individual anode wires. Charged particles passing through the cells induce signals on the wires. The cells are operated in the proportional region to enhance the rate handling capability and to reduce the aging effects. The gas used will be a mixture of Ar and CO_2. A small amount of CF_4 gas will be added to get fast drift times of the order of 80 ns. δ-electrons reaching neighbouring cells are stopped by the separator walls, thus reducing cross-talk. These detectors can be built with a small amount of material, typically 1% X_0. Most of the charged particles are expected to fire only one cell.

The hexagonal common cathodes are connected to the negative HV supply and the wires are grounded individually through the inputs of the readout chip. The chip has suitable performance specifications to handle low proportional signals from the wires of the cells.

The layout of the CPV along with its stand and the inside view showing the honeycomb structure is shown in Fig. 4

2.3.2 Simulation

Simulation of the electrical field distribution in hexagonal geometry with a sense wire at the centre of the cell has been performed using GARFIELD code [29]. Fig. 5 shows uniform field configurations in the central section of the cell with almost circular equal-time contours extended to more than 3/4 radial distance [30]. Addition of a few percent of CF_4 completely eliminates the long tails in the signal and produces sharply peaked output. The entire charge is collected within 80 ns. The efficiency of detection of charged particles, assuming 0.2 MIP as noise threshold, is found to be almost 100%. The MAGBOLTZ plot of drift velocity vs E/p shown in Fig. 6 indicates a plateau between 1–10 E/p range. GEANT simulation has been done to study the influence of material on δ-electrons. It is found that approx. 0.2 mm thickness of any suitable material is adequate to contain most of the δ-rays within one cell.

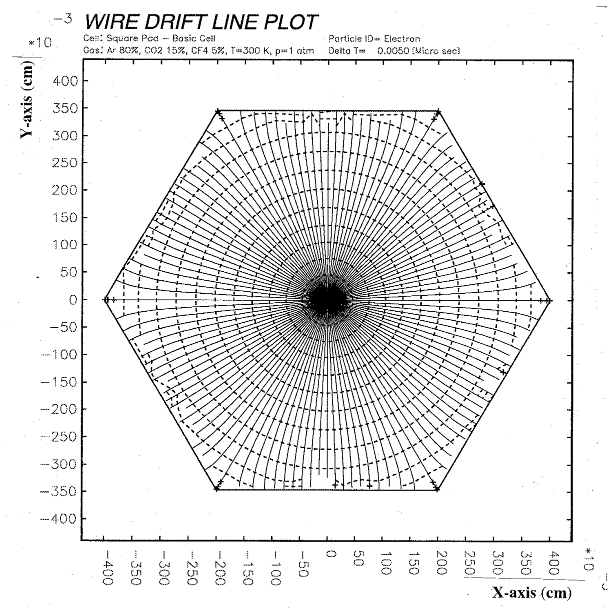

Figure 5: Plot of equipotential lines for a hexagonal cell with sense wire at the centre.

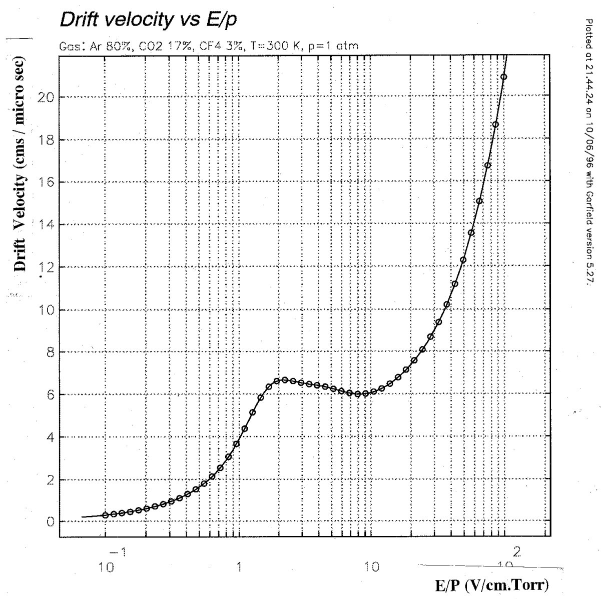

Figure 6: Drift velocity vs E/p plot for the hexagonal cell.

2.3.3 Electronics and Readout

The readout of the wire signals will be done using the GASSIPLEX chip developed at CERN [31]. The 16-channel chip shown schematically in Fig. 7 (a) is composed of a charge sensitive amplifier (CSA), a switchable filter (SF) and a Track/Hold (T/H) stage to store charges in a capacitor by operating switches #1. Test pulses can be sent to all the channel inputs through a calibrated test input line. Sending control signals (Track/Hold, train of clock pulses and reset) allows the multiplexed read out of stored charges on a single output line by sequentially operating the switches #2.

Since gassiplex is a an ungated asynchronous device its inputs and outputs are always in live state. Hence each output or the base line has to be kept at a constant dc level (called pedestal) in the absence of input signal. The mean value of this is adjusted close to zero in order to take advantage of the full dynamic range of the device. This can be set in either polarity depending upon the ADC used. By variation in the pedestal level we can find out the noise figure of that channel. Depending on input capacitance this number is equivalent to few tenths of fc or few hundred of electron rms.

The charge sensitive amplifier is characterised by a long integrating time (600–800 ns) with a sensitivity (12 mv/fc) providing very high performance in detecting very low level signals, thus allowing efficient single electron detection. The peaking time is of the order of 700–800 ns and is used as natural delay to wait for external trigger decision .

At the occurence of an event the capacitors associated with hit channels are charged up by corresponding detector currents. An external signal synchronous to that event is used to generate a HOLD signal to the entire system opening all the switches at a time corresponding to the peaking time of the shaping amplifier. Therefore maximum signal charges are stored for the hit channels. Charges corresponding to their pedestal values are stored for those having no hit. As long as HOLD signal is maintained ON the switches are open and the charges stored in the capacitors. They are lost when HOLD is released. In operation mode the switches driven by the T/H stage are closed and those driven by the MPX stage are open.

The decision for read out of an event is independent of T/H operation. For this a Start signal is generated from the event trigger with a suitable delay.

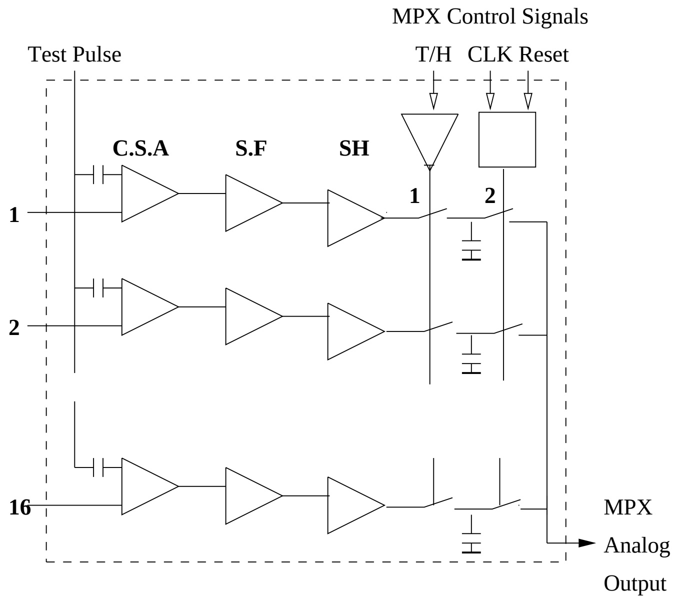

(a)

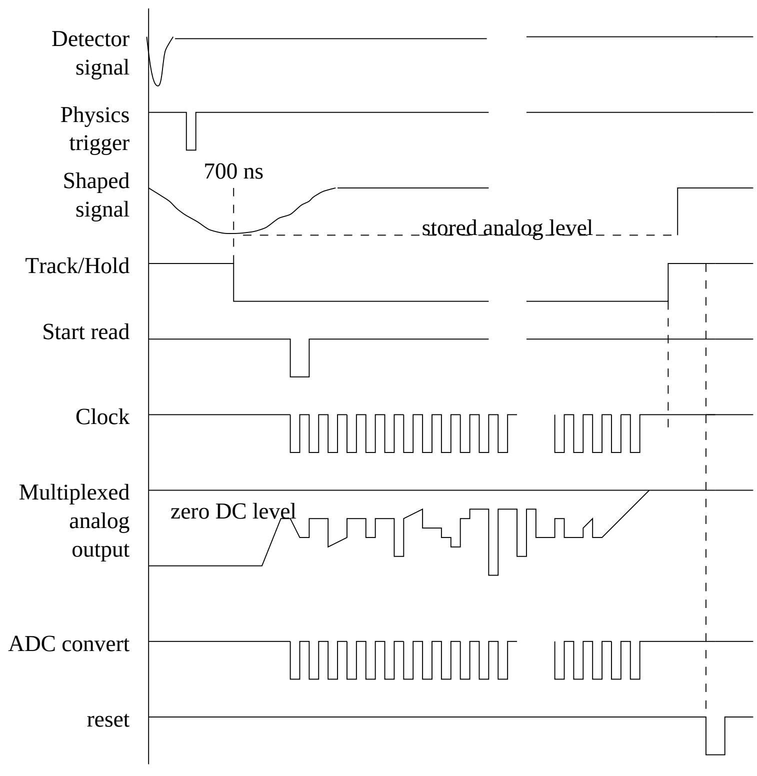

(b)

Figure 7: (a) Schematic of the functional blocks of gassiplex chip, (b) Timing diagram for gassiplex operation.

This starts a chain of MPX clock pulses from an external device (the sequencer) allowing adjustment of the number and frequency of clock pulses. As soon as the clock train is over and the digitizations performed, a RESET signal is sent to gassiplex which resets all the switches to initial positions. This can be sent after the HOLD signal is released.

Fig. 8 shows the schematics of the readout system for a daisy-chain of gassiplex chips, referred as a block. The system generates a set of NIM signals : T/HOLD, RESET and an adjustable level via an attenuator for calibration and testing purpose to be distributed to gassiplex boards and a Start Read signal (NIM) to the read out system to start clock train pulses (NIM) with manual adjustable delays. These can be generated by normal NIM electronics. The system converts the NIM levels of the control signals into levels required by the gassiplex by a LEVEL SHIFTER card, duplicates the control signals to allow parallel operation of many blocks using REPEATER cards and also distributes the low voltages required (0, +3.5 V) to all the elements of the readout blocks. The Buffer Amplifier is required for transmission of analog multiplexed train to the read out module with provision for base line adjustment for either polarities.

As a baseline option, the readout system for the gassiplex chips will be based on commercially available VME Modules : the CAEN Model V 550 C-RAMS and Model V 551 C-RAMS SEQUENCER with the following features.

C-RAMS (CAEN Readout for Analog Multiplexed Signals) : This module consists of two independent conversion blocks, each having capability to handle 2016 channels in steps of 32. Thus a maximum of 126 gassiplex chips can be daisy-chained to be readout using one block of the C-RAMS. It has 10-bit ADC and 200 ns conversion time. It includes memories for loading pedestal levels and threshold values and zero suppression upto 5 MHz and FIFO memory for storing digitization and address of data above threshold. 2000 channels can be read out in about 1 to 1.5 ms depending on the parasitic capacitance of the daisy chain.

C-RAMS Sequencer: This module can control upto 19 C-RAMS modules in a complete VME crate enabling the readout of upto 76608 detector channels and is controlled via a VME bus. The multiplexing frequency can be set via VME from 100 KHz to 5 MHz.

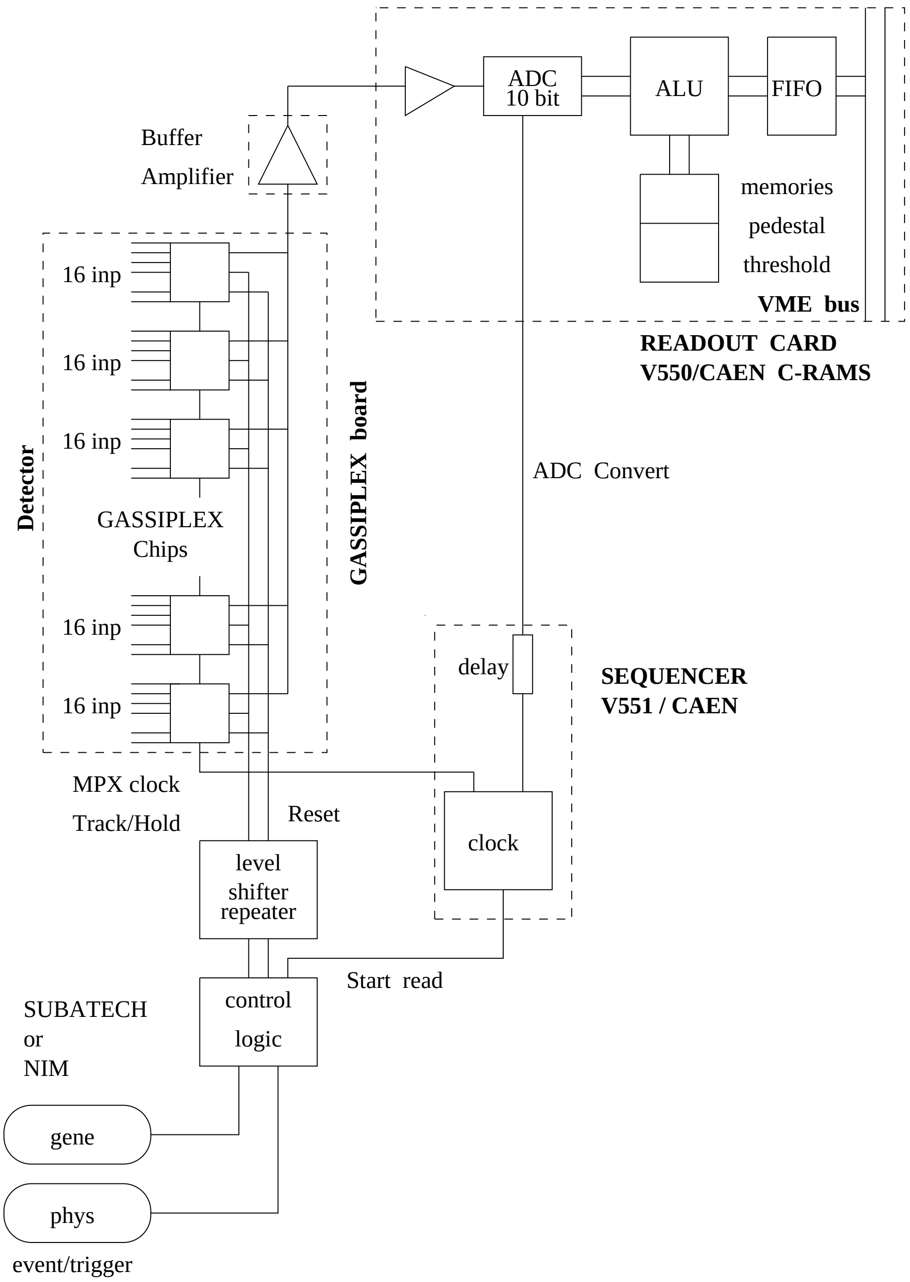

Figure 8: Schematic of GASSIPLEX chain readout system.

3 Simulation

The PMD will be placed in the forward rapidity region at a large distance from the vertex to be able to handle the high particle multiplicity. Several detector subsystems of STAR interpose materials in front of the PMD. Hence a detailed simulation has been carried out to study the effect of materials with special reference to the capability of the PMD for event–by–event physics, role of charged particle veto, the efficiency of photon counting and the rejection of background.

3.1 Simulation Framework

The detector characteristics have been studied using GEANT simulation within the framework of the GSTAR package.

3.1.1 Particle Species

Two approaches have been undertaken.

(a) Single particle simulation : A large number of photons , π^+, and protons of varying energies were directed towards the PMD from the interaction point. From this study we obtain the conversion probability of photons and the background being produced due to the interaction of hadrons in the thick converter and other upstream materials and also due to upstream conversion of photons.

(b) Simulation with event generator : VENUS 4.12 event generator has been used to generate particles for the simulation in the high multiplicity environment. Here we study the role of materials with special reference to the suitability of the PMD for event–by–event physics. The particle density obtained with this event generator is one of the highest so far in comparison to other (FRITIOF, HIJING, HIJET etc) event generator outputs at the RHIC energy. Hence this study should give possibly worst case performance of the detector. Default values of the parameters are used in VENUS and all the unstable particles and resonances are allowed to decay at the generator level.

3.1.2 GEANT parameters

The physics processes switched ON during simulation were :

DCAY, ANNI, BREM, COMP, HADR, MUNU, PAIR, PHOT, RAYL, LOSS, DRAY, MULS, STRA.

Energy cutoff used for the secondary particles while passing through the PMD material was kept as 100 KeV. For the upstream materials default values as provided in GSTAR were used.

3.1.3 Geometry Implementation in GSTAR

The detectors and associated materials which are foreseen to be present in front of the PMD are,

(a) Magnetic field,

(b) Magnet poletip,

(c) Forward TPC, support structure and electronics,

(d) Silicon Vertex Tracker (SVT), water manifold and associated support structure.

(e) Beam pipe.

The effect of the main TPC is negligible. We have not considered the vertex position detector (VPD) in our simulation , as **it has been agreed upon to position the VPD in the central hole of the PMD** [42]. In such an arrangement, the VPD does not introduce any material in front of the PMD.

For the simulation , the geometry files for the various subsystems were taken from the GSTAR library as provided by the respective groups. For the beam pipe different compositions have been studied : (i) entire length (upto the position of the PMD) made of Beryllium, (ii) 76.2 cm of Beryllium and the rest of Aluminium and (iii) 76.2 cm of Beryllium and the rest of SS.

PMD Geometry in GSTAR

The PMD consists of two sensitive volumes :

(a) 3 mm thick scintillator as the sensitive medium of the preshower part, and

(b) 8 mm Argon gas as the sensitive medium of the CPV.

Separation between the front faces of the gas and the scintillator was taken as 3 cm. The materials placed in between these two sensitive media are,

(i) 1.7 cm of Pb as the converter ($3X_0$), and

(ii) 0.5 cm of Fe as the support structure.

Each sensitive medium was divided into two sets of boxes,

(a) 12 boxes of dimensions 61.4 cm $\times$ 76.6 cms at larger angles, and

(b) 12 boxes of dimensions 46.8 cm $\times$ 58.4 cms at smaller angles.

The boxes were rotated properly to place them inside the PMD volume. The final shape of boxes in the PMD are shown in Fig. 1.

3.2 Study with single particles

Simulation has been performed using 5000 particles each of photons, π^+s and protons having longitudinal momenta (p_z) of 0.5, 1, 2, 5 and 10 GeV/c. All the detector subsystems described above were used. The beam pipe was assumed to be made up of Beryllium only.

Two separate η–regions have been studied :

(a) The region $2.0 \leq \eta \leq 2.8$ on the outer part of the PMD where FTPC presents substantial material in front of the PMD, and

(b) The region $3.0 \leq \eta \leq 3.4$ in which the upstream material is relatively less.

The conversion probability ϵ_{conv} of photons is obtained by computing the fraction of incident photon tracks giving signal above a preselected threshold. From a comparison of the number of incident particles giving signal and the cluster multiplicity obtained after performing clustering on simulated data, the number of extra clusters generated due to the upstream conversion is estimated. These quantities are studied for different thresholds on cluster signal to understand the effect of threshold in reducing the background.

Fig. 9(a,b) show the conversion efficiency of photons for different thresholds on cluster signal for the two η–regions considered. After 3 MIP (1800 KeV) threshold, the conversion probability of 1 GeV photons is of the order of 80%.

The usefulness of the CPV is studied using the following simple vetoing algorithm.

If any one of the neighbours in a 3 × 3 matrix around the preshower cluster position is having non-zero energy deposition in CPV, then we veto that cluster.

If we consider the effect of threshold together with the effect of vetoing then in addition to the reduction in background, photon conversion probability also reduces. Because of the upstream conversion of the photons, the shower particles (electrons and positrons) produce hits on the CPV also and hence the clusters are vetoed.

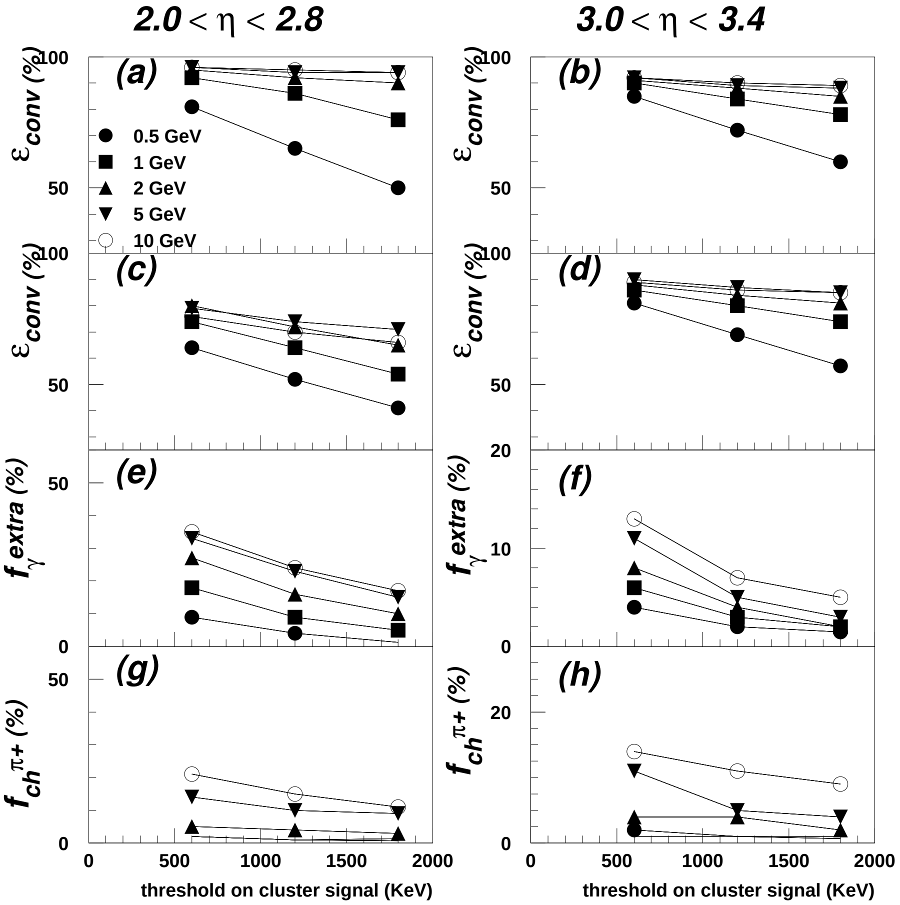

Figure 9: (a), (b) : Conversion probability (%) of photons before using veto;
(c), (d) : Conversion probability of photons after veto;
(e), (f) : Fraction of extra clusters after veto; and
(g), (h) : Fraction of π^+ remaining as background after veto.

We have calculated the percentage of clusters forming the part of extra clusters generated from upstream conversion of photons. Extra cluster multiplicity has been obtained by taking the difference between the cluster multiplicity above threshold and the number of tracks giving signal. Number of clusters vetoed are then subtracted to obtain the extra clusters which form part of the background after veto.

Fig. 9 (c,d) and Fig. 9 (e,f) also show respectively the results for conversion probability and extra cluster fraction f_{γ}^{extra} after veto for the two η–regions. The conversion probability after veto is found to be somewhat lower as compared to that shown in Fig. 9 (a) in the low η–region. For 1800 KeV (3 MIP) threshold, the conversion probability for 1 GeV photons remains more than 75% for high η–region but reduces to 65% for low η–region. Using 3 MIP threshold only 1.8% of the clusters are observed as the extra clusters for 1 GeV photons in the high η–region, while for low η–region this numbers goes up to 6%.

Fig. 9 (g,h) show the fraction $f_{ch}^{\pi^+}$ of incident π^+ which remains as the background after vetoing with the CPV signal. For any threshold on cluster signal, only about 2% of 1 GeV π^+ remain as background in the high η–region. The fraction goes up to 3-4 % in the low η–region. Similar results were also obtained for protons, with at most 2% of protons remaining as background. We are therefore hopeful that with the use of the proper vetoing algorithm, most of the hadrons ($> 90\%$) will be vetoed.

3.3 Study with Event generator

VENUS events were passed through GSTAR to study the capability of photon detection with the PMD in high multiplicity environment and estimate the photon counting efficiency and background fraction as defined in Eqns. 5 and 6. To demonstrate the effect of different detectors, we used the PMD in combination with these detectors in isolation and also all put together.

Fig 10 shows the N_{γ}/N_{ch} ratio for 50 VENUS events in the PMD acceptance. This ratio is important from two considerations : (i) N_{γ}/N_{ch} is the simplest observable for the study of the DCC and isospin fluctuations. It is thus important to know the fluctuations present in the normal events. (ii) In a photon multiplicity detector, the background is directly related to N_{ch}. Thus a knowledge of the fraction of charge particles present in the event gives an idea of the background

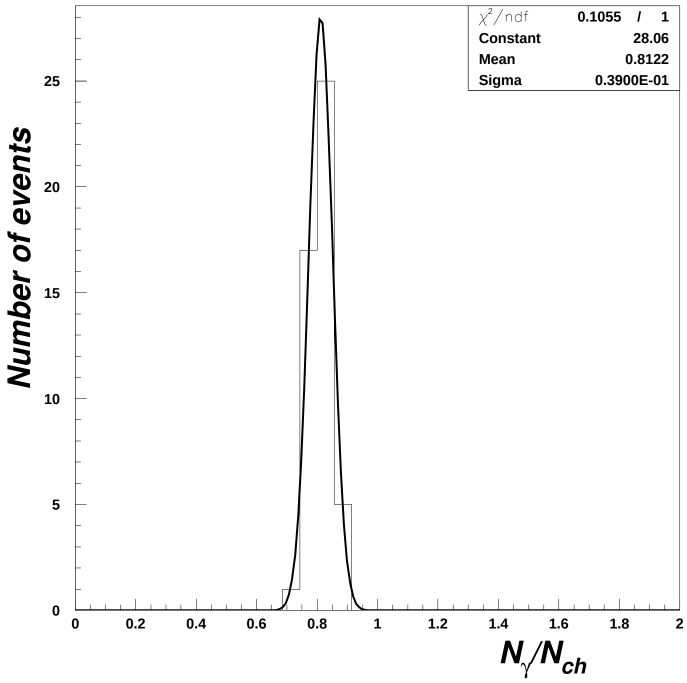

Figure 10: N_γ/N_{ch} for raw VENUS events in the acceptance of the PMD. Note the small σ of $\sim 5\%$.

on the detector in the case of a normal event. It is found that the event-to-event fluctuation in N_γ/N_{ch} ratio in the generic event is of the order of 5%.

3.3.1 Occupancy and Multiple Hit Probability

The number of pads fired in central events gives us the idea about the pad occupancy. Inclusion of new materials in the setup will increase the pad occupancy due to the increase in the number of converted photons and increase in charged particles falling on the detector due to multiple scattering. Knowledge of pad occupancy is also important from the point of view of data volume to be expected in PMD in central collisions.

Another quantity investigated is *multiple hit probability*. This represents the fraction of fired pads which are hit by the secondary particles belonging to more than one incident tracks. This will give us an idea about the difficulty in handling the data in crowded environment. It has been found earlier that the clustering inefficiency is directly related to the multiple hit probability [32]. For an event with low multiple hit probability, we can perform clustering better.

TABLE II

Occupancy and Multiple Hit Probability

Case	Configuration	mulh(%)	N_γ	N_{ch}	O$_P$ (%)	O$_C$(%)
1.	PMD in Cave	4.8	908	1172	8.2	3.2
2.	PMD in Cave with Poletip	5.0	926	1234	8.4	3.5
3.	(2) + SVT	5.1	933	1240	8.6	3.8
4.	(2)+ FTPC	5.5	890	1239	9.8	4.8
5.	(2)+ Be-Pipe	6.2	946	1255	10.0	6.1
6.	(2)+SVT+FTPC+Be-Pipe	7.1	974	1436	12.6	8.5

Table II shows multiple hit probability (mulh) and pad occupancies for the PMD (O$_P$) and the CPV (O$_C$) along with the number of photons (N_γ) and charged (N_{ch}) tracks giving signal on the detector for various configurations. Starting with the simplest configuration of the PMD alone in the Cave, we have added various subsystems one by one to study their effects. It is seen that the pad occupancy increase from 8% to 13% in the preshower section of the PMD and from 3% to 9% for the CPV as more and more materials are added. This is caused by the upstream conversion of photons producing secondaries which arrive at the PMD over a large area. It is also seen that the rate of increase in pad occupancy is higher for CPV compared to that in the preshower part. The pad occupancy in the preshower part is dominated by the number of photons and is already reasonably high for the PMD alone. Addition of materials increases the number of charged particles significantly but the number of photons increase only marginally. Thus in the case of preshower part mostly the pads fired earlier by shower particles are getting affected again, while in the case of CPV new pads are getting fired thereby increasing the pad occupancy.

3.3.2 Clustering and Track Identification

The simulated data obtained in the form of energy deposited in pads were processed through a clustering routine in order to obtain the clusters of pads affected by a single track. For the present report, we have adopted the method of finding the local maxima followed by splitting of clusters. We call a pad to be the location of a *local maxima* if it is at the centre of a 3×3 matrix having energy deposition higher than neighbouring 8 pads. For a cluster having more than one local maxima, we split the energy deposition of the pad common to all the maxima according to the distance of the pad from the maxima.

We assign the identification of the clusters according to the track depositing energy on the local maxima. From the corresponding track number we obtain the information about the tracks forming more than one clusters.

3.3.3 Effect of Materials

Because of the presence of materials in front of the PMD following things can happen :

(a) Tracks originally directed away from the PMD region will get scattered and converted in the materials and the secondaries will fall on the PMD surface. This effect is more prominent in the large η–region due to the beam pipe.

(b) Photon tracks directed towards the PMD get converted in the upstream materials and the secondaries form separate clusters with signals also on the CPV. This effect is more in the low η–region because of the presence of the FTPC.

We have studied the effect of various materials using VENUS events also. Fig. 11 shows the background fraction due to extra photon clusters and due to tracks originating outside the acceptance of the PMD. It is clearly observed that the effects due to beam pipe and the FTPC contribute in complementary η–regions. It is thus expected that the overall background may be uniform over the η–acceptance of the PMD.

Fig. 12 shows the background fraction arising from tracks outside the PMD acceptance for various beam pipe configurations. It is seen that while there is no substantial increase in background in going from the option of beam pipe made entirely of Beryllium to the option of Beryllium + Aluminium, the background suddenly shoots up with the introduction of the SS section. Similar effect has been observed by the FTPC group and concern has been voiced against the use of the SS option [33].

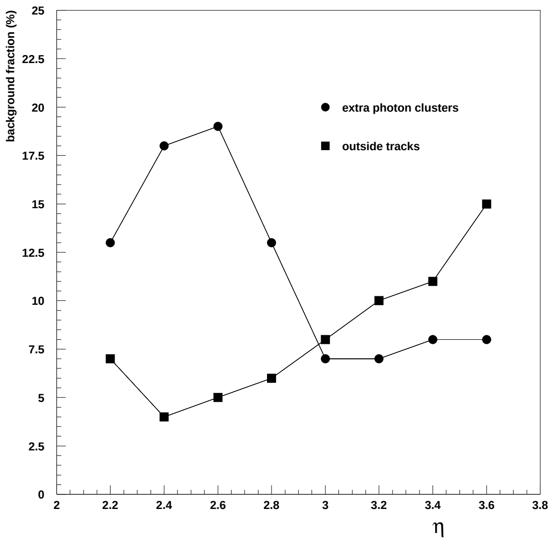

Figure 11: Contribution to the background fraction from FTPC and from beam pipe in different η regions shown separately in terms of extra photon clusters and of tracks outside the PMD acceptance.

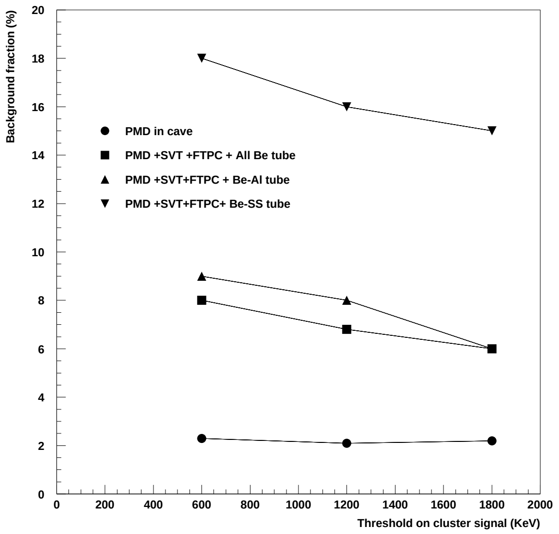

Figure 12: Background arising from tracks outside the PMD acceptance due to different beam pipe structures.

3.3.4 Guidance for Event–by–Event Physics

For event–by–event physics to be possible using the PMD it is not only sufficient that photons are detected with good efficiency and there are lesser background contaminants, but in addition it is also required that photon tracks are not deflected significantly from their original direction. Because of the presence of upstream materials, some tracks will get deflected. We consider a photon cluster to be a good cluster, when the cluster is confined within certain $\delta\eta$ and $\delta\phi$ range, where $\delta\eta = \eta_{cluster} - \eta_{original}$ and $\delta\phi = \phi_{cluster} - \phi_{original}$ measure the deviations of the original direction of the track with respect to the measured cluster position. From the study of the single particle simulation, we have learnt that $\delta\eta = 0.1$ and $\delta\phi = 20^0$ is a reasonable choice. Setting tight limits on $\delta\eta$ or $\delta\phi$ may exclude the photon clusters appearing separated due to the effects of granularity.

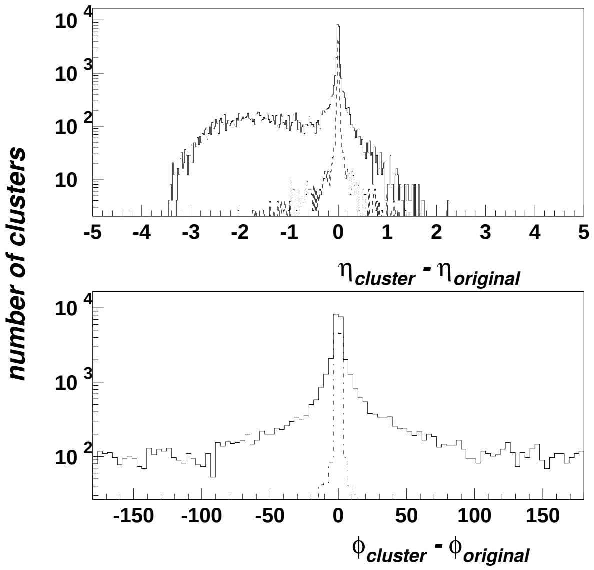

Figure 13: Distribution of $\delta\eta$ and $\delta\phi$ for VENUS generated photons. The dashed line represents the PMD alone in cave, the outer envelope shown with solid lines represents the PMD in the presence of all other materials. For visual clarity the solid line curve is plotted with an y-axis offset of 1000.

Fig. 13 shows the distribution of $\delta\eta$ and $\delta\phi$ for photons for the two cases

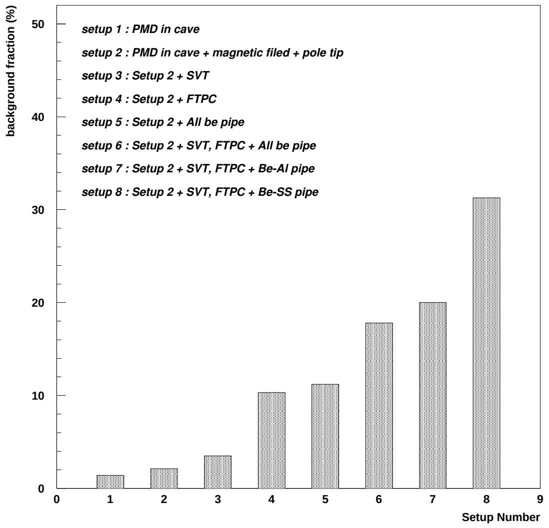

Figure 14: Fraction of photon tracks outside the range of $\delta\eta < 0.1$ $.and.$ $\delta\phi < 20^0$ for various cases as indicated.

: (a) PMD alone in the Cave and (b) PMD in Cave with magnetic field, magnet poletip, SVT, FTPC and the Be–SS beam pipe. The large tilt of the $\delta\eta$ histogram towards negative values for the second case with all the upstream materials indicates that particles travelling within the beam pipe at larger pseudo-rapidities get scattered in the material of the beam pipe and land at the PMD at smaller pseudo-rapidities. Although the $\delta\phi$ histogram is largely symmetrical because of the azimuthal symmetry of the event and the detector, the fraction of particles going at large $\delta\phi$ increases considerably with the introduction of the materials.

The fraction of photon tracks having deviations larger than the selected limit is shown in Fig. 14 for the case of PMD alone and in the presence of other materials. The usual threshold of 1800 KeV was applied on the cluster signal. It is seen that the track deviations gradually become more as more materials are added, with significant jumps at the addition of FTPC (setup 4) and the beam pipe (setup 6). There is no significant difference between the Beryllium and Beryllium–Aluminium pipe. The fraction of deviated tracks are still within 20%. However the addition of SS section to the beam pipe increases this fraction to more than 30% which is rather very high. For reasonable event–by–event physics we feel that the use of Beryllium–Aluminium beam pipe will be more practical.

The $\delta\eta$ and $\delta\phi$ values limit the capability of the PMD for any differential analysis at much smaller scales. Very small bins in η and ϕ have problems of too few particles and correspondingly higher statistical fluctuations. Thus for a meaningful analysis coarse binning is preferable. It is difficult to predict the scale at which fluctuations will become visible. Pairing and clustering of tracks were observed in very high multiplicity events of JACEE experiment [34] at scales $\delta\eta \sim 0.2$ and $\delta\phi \sim 30^0$. This observation along with theoretical suggestions [7] indicates that our choice of $\delta\eta$ and $\delta\phi$ bin sizes will be adequate for event–by–event studies of fluctuations.

3.4 Vetoing using Neural Network Technique

For the purpose of reducing the background we plan to implement the Charge Particle Veto (CPV). For the single particle studies we used a simple vetoing algorithm with success. However in the high multiplicity environment of the actual event such a simple algorithm may not effectively work.

Neural Network (NN) has been extensively used to solve problems of high degree of complexity, such as feature classification, image processing, pattern recognition, combinational optimisation etc. Neural network is also being used for pattern recognition in high energy physics extensively. One of the specific examples is to discriminate different type of shower particles in a calorimeter. But these applications are mostly limited to low multiplicity events. We have attempted to use the NN technique for the discrimination of photon and hadron clusters in the preshower PMD in a truly high multiplicity environment.

We have used two–layer network consisting of one hidden layer to solve the problem. Jetnet 3.4 [35] has been used for the above purpose. Response function used is of the form $F_c(X) = \frac{1}{1+e^{-X}} == F_c(x, w)$, where x's are the given inputs and w's are the corresponding weights. F_c varies between 0 to 1. Target values (F_{known}) for photons and hadrons are set to 0 and 1 respectively.

Network has been tested for the response of the detector with single particles and with VENUS events. Following inputs were given to the network, one set each for the Preshower part and the CPV respectively.

(i) Fraction of signals in 9 pads around the maxima of the profile of the energy deposition by a particle (x_1 to x_9).

(ii) Total energy deposition by the particle (x_{10}).

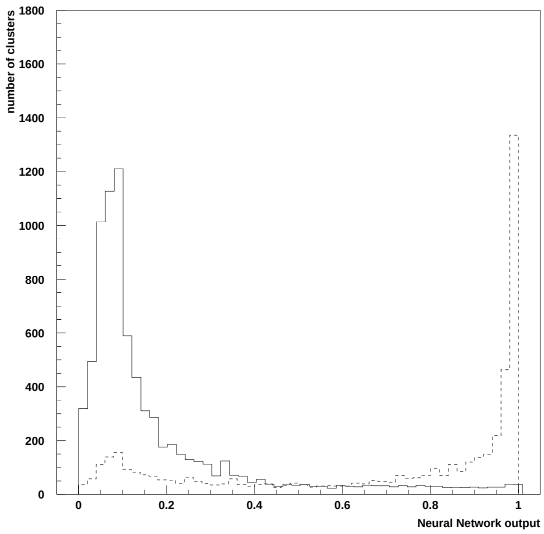

Figure 15: Network output spectra for VENUS particles using JETNET 3.4. Solid histogram represents photons and dashed histogram represents hadrons.

(iii) Total number of pads affected by the particle (x_{11}).

The performance of the network was judged for the VENUS events by computing the two quantities ϵ_γ and f_{bkg} defined earlier using Eqns. 5 and 6. Definitions used for signals and for backgrounds were the same for training as well as for testing.

The shape of the NN output spectrum is shown in Fig. 15 for the case of PMD alone placed in the cave. The solid line indicates photons and dashed line the background. It is observed that a network threshold of about 0.5 will remove most of the backgrounds and also ensure reasonably large photon counting efficiency.

The performance of the network using Jetnet 3.4 is summarised in Table III for the various configurations studied. From Table III we observe that the photon counting efficiency remains $> 70\%$ so long as the beam pipe has not been included and afterwards starts falling. The reduction in efficiency with the inclusion of beam pipe is mainly due to increased pad hits in the CPV which leads to proportionately increased vetoing of photon clusters. With all the detector components in place, we achieve a photon counting efficiency of 65.5% associated with a background contamination of 35.5%. Both these values are very close to

TABLE III
Performance of network using Jetnet 3.4 for different setups, using a network threshold of 0.55 with the inputs taken from preshower detector and CPV.

case	Configuration	ϵ_γ(%)	f_{bkg} (%)
1.	PMD in Cave	73.7	16.6
2.	PMD in Cave with Poletip	72.5	17.8
3.	(2) + SVT	71.0	20.2
4.	(2)+ FTPC	70.5	26.6
5.	(2)+ Be-Pipe	66.5	29.5
6.	(2)+SVT+FTPC+Be-Pipe	65.5	35.5
7.	(2)+SVT+FTPC+Be-Al Pipe	65.5	37.5

those obtained in the case of WA98 PMD. Even using more realistic beam pipe of Beryllium + Aluminium seems acceptable. This result is very encouraging as the effective signal threshold for hadron rejection in this case is much lower than that in the method of WA98 PMD for obtaining similar background. This will greatly help in retaining low p_T photons in the event as described in the next section and will enhance the potential for DCC searches.

One of the modifications in the Neural Network approach could be the use of multiple output nodes separately for multiple background types, e.g., hadronic background and upstream photon conversion. We are working on improving the vetoing algorithm, which will hopefully reduce the background to $\sim$ 20% level.

4 Capabilities of the PMD

4.1 Photon Counting Efficiency and Background

Our present estimate of the average photon counting efficiency and average background fraction (which were defined earlier in Eqns. 5 and 6) from simulation studies and using NN algorithm for removing hadrons is 65.5 % and 35.5% in central collision events in the actual environment of the STAR experiment with all the subsystems in place. Fig. 16 shows the variation of photon counting efficiency and background fraction for the full η–region covered by the PMD. It is seen that despite the presence of varying degrees of materials in different η–regions, both the efficiency and the background are fairly uniform over the entire

η region. This clearly suggests that the PMD can be implemented in STAR and will work along with all the other detector subsystems. Attempts to reduce the materials will be always welcome.

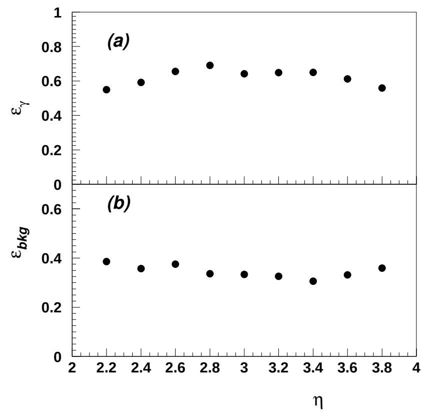

Figure 16: Photon counting efficiency and background fraction for the STAR PMD as a function of η.

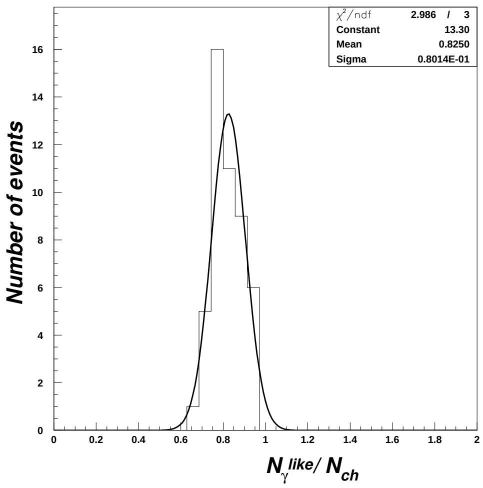

Figure 17: $N_{\gamma-like}/N_{ch}$ for the real case of PMD after simulation, assuming 99% charged particle detection efficiency in the FTPC and the actual photon counting efficiency. Note that $\sigma < 10\%$.

An idea of the event–to–event fluctuations in the measured N_γ/N_{ch} can be obtained from Fig. 17 which shows the ratio plotted for the real case of the PMD after simulation, assuming 99% efficiency for charged particle detection and the actual efficiency for photon counting. If we compare the $\sigma < 10\%$ for N_γ/N_{ch} obtained in this case with that of 5% obtained for raw VENUS numbers as shown in Fig. 10, we find that the extra fluctuation introduced by the detector is quite reasonable and it should be still possible to study large fluctuations on event–by–event basis.

4.2 Low p_T Selection

For the study of DCC–related phenomena, one would like to have almost pure sample of low p_T particles [1]. For photons this is possible only by using an e.m. calorimeter. The signal from the preshower detector has large fluctuations and it is not possible to extract the energy of photons for individual particles. The fluctuation reduces considerably when the preshower signal is summed over a group of particles. This idea has been used in the estimation of E_T^{PMD} as described in the next section.

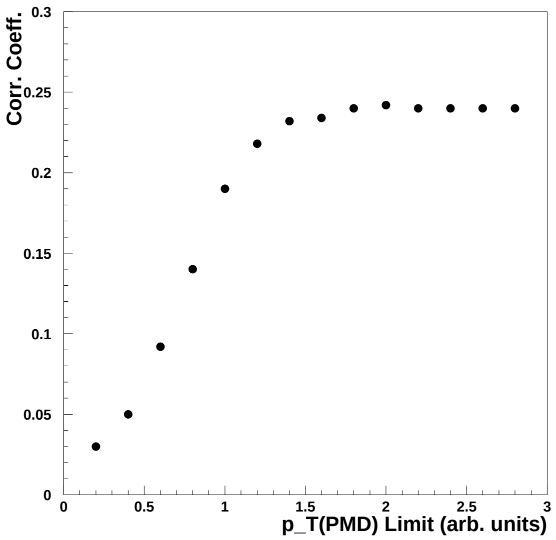

Figure 18: Correlation between p_T and p_T^{PMD} for a range of values of p_T^{PMD}(limit) and for $p_T < 200$ MeV/c.

We have tried to explore the possibility of cumulative selection of particles having $p_T < p_T^{max}$, where p_T^{max} is in the range of 100–300 MeV/c, suitable for DCC searches. We compute the quantity $p_T^{PMD} = \Delta E.\ \sin\theta$ where ΔE is the preshower signal of the photon cluster appearing at angle θ on the PMD. For individual particles there may not be any visible correlation between p_T and p_T^{PMD}. However considering a group of particles with $p_T < p_T^{max}$ and $p_T^{PMD} < p_T^{PMD}(limit)$ a small but significant correlation is found between the two variables. Fig. 18 shows the correlation coefficient between the original p_T of the particle and the p_T^{PMD} computed from the preshower signal for a range of cuts on p_T^{PMD}. The correlation coefficient is calculated in the usual way and summation runs over the set of particles having $p_T < p_T^{max}$ and $p_T^{PMD} <$ the chosen values of p_T^{PMD}(limit). It is seen that as the limit on p_T^{PMD} is increased to include more and more particles of the same p_T class, the value of the correlation coefficient increases and then saturates. The saturation indicates that no further inclusion of particles of that class is taking place. Selecting on particles having suitably-chosen p_T^{PMD} range should then enhance the sample in low p_T particles.

For generic events the fraction of low p_T photons in the event is usually 30–50% depending on the value of p_T^{max}. Let us consider :

Signal (S) = fraction of low p_T photons in the range of interest.

Background (B) = rest of the photons in the event.

When no selection is applied we have a sample of N photons consisting of N_S signal photons (with p_T within the selected range) and (N–N_S) background photons. Since in this sample all the N_S signal photons are present we call the selection efficiency of signal as 100%. We now produce another sample (from the set of photons in the same event) of N' photons which has N'_S signal photons and (N'-N'_S) background photons by making suitable selection on the value of $p_T^{PMD}(limit)$. In this case the selection efficiency is $\mathrm{N}'_S/\mathrm{N}_S$ and the S/B ratio is $\mathrm{N}'_S/(\mathrm{N}'$–$\mathrm{N}'_S)$. The aim of the present selection scheme is to maximise the S/B ratio while maintaining high selection efficiency of the signal.

Fig. 19 shows the relation between the selection efficiency and the S/B ratio for selecting photons with $p_T <$ 200 MeV/c in a set of VENUS photons detected by the PMD above a certain threshold on the cluster signal as indicated. Substantial improvement in the S/B ratio is observed even for moderately high selection efficiency. Even if large hadron rejection threshold is applied the relative improvement in the S/B ratio compared to the no-selection case seems to grow better. However application of large threshold for hadron rejection reduces the absolute number of low p_T particles in the event. In the VENUS events the fraction of detected photons with p_T < 200 MeV/c reduces by $\sim$ 18% at a threshold of 600 KeV but becomes almost half at a threshold of 1800 KeV. It is thus prudent to work with smaller thresholds and more intelligent algorithms for hadron rejection, as described in Sec. 3.4, to retain the large multiplicity of low p_T particles.

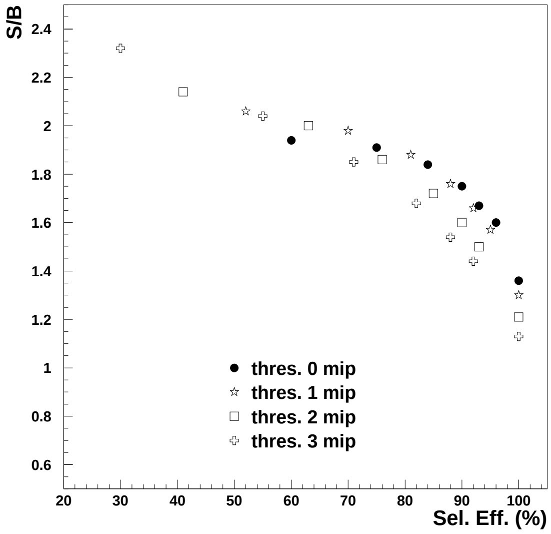

Figure 19: Signal-to-Background ratio for selecting photons with p_T <200 MeV/c as a function of selection efficiency and for various thresholds on the cluster signal as indicated. 1 MIP = 600 KeV.

Table IV presents the S/B ratio for 80% selection efficiency of photons in various low p_T ranges as indicated after applying 600 KeV threshold on the cluster signal. For comparison the S/B ratio for the unselected sample is also shown. It is clear that the selection procedure improves the S/B ratio by $\sim$50% in almost all the ranges.

TABLE IV

S/B Ratio for selecting different p_T ranges with $\sim$ 80% efficiency.

p_T^{max} (MeV/c)	S/B (Eff.=80%)	S/B (no selection)
100	0.59	0.38
150	1.14	0.78
200	1.88	1.30
250	2.76	1.94
300	3.88	2.74

Such an enhancement of low p_T samples will be of great help in searching fluctuations using the Wavelet method [36, 37] which is very sensitive to the differential distributions in the event. Larger S/B ratio is obtained when the efficiency of selection is lower. Maximum sensitivity to any fluctuation observable is expected to be obtained only after detailed study of samples which are purer in low p_T particles but the total number of particles is still large enough so that statistical fluctuations do not dominate. For the results presented above only photon clusters on the PMD have been considered. Effect of admixture of hadronic secondaries is not expected to worsen the results significantly as the effects persist even at large thresholds.

The sensitivity of the PMD for low p_T photons extends down to < 20 MeV/c [26]. As the FTPC will provide p_T selection for charged particles, the PMD–FTPC combination should become an ideal tool for searching any physical processes leading to charge-neutral fluctuations.

4.3 Search for DCC

One of the important objectives of implementing the PMD in STAR is to search for the DCC. Although at present we have not tested the effectiveness of the PMD using any DCC event generators, we have studied the response of the PMD to enhancements in the input photon multiplicity while keeping the hadronic background unchanged. This has been done by throwing a fraction of photons from the -ve p_Z direction to PMD direction (+ve p_Z) within the PMD acceptance. The number of photons added from the -ve direction was 5%, 10% and 20% of the multiplicity of photons present in the +ve direction within the acceptance of the PMD.

The modified events were passed through GSTAR simulation and the clustering and photon selection has been done by the usual method described earlier. Fig. 20 shows the observed cluster multiplicity $N_{\gamma-like}$ for various input photon multiplicity N_γ in the event. It is seen that there is a clear correlation between the detected $N_{\gamma-like}$ and N_γ for the events with even 20% extra photons as presently studied. This demonstrates the capability of the PMD for the DCC physics in the actual environment of STAR.

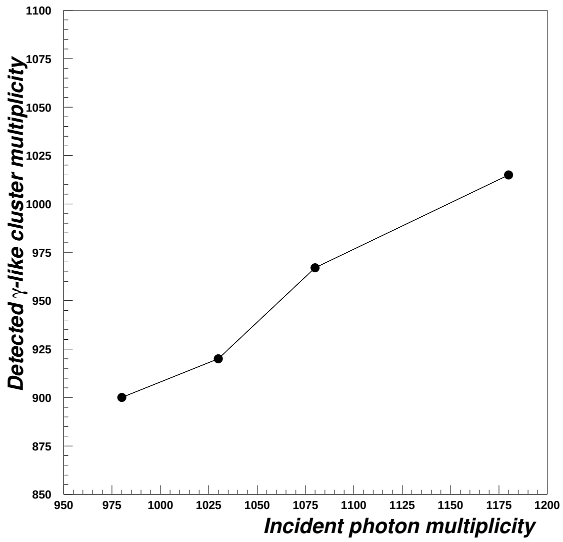

Figure 20: Detected γ-like cluster multiplicity for the modified events with incident photon multiplicity enhanced by different fractions (0.0, 0.05, 0.1, 0.2) over the normal event.

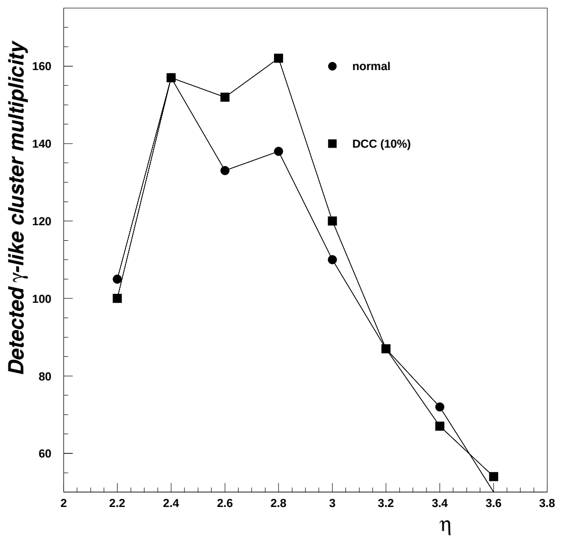

Figure 21: Number of detected γ–like clusters in various η–bins in the normal (filled circles) and modified (filled squares) events. No correction has been applied for geometrical acceptance at various η.

To test the possibility of detecting the enhancement of photon multiplicity in a selected η region, as could possibly arise in the case of DCC formation, we included 10% additional photons to the normal event in the region $2.4 \leq \eta \leq 3.2$. This region was selected to test the response of the PMD where the FTPC interposes more material. The η-distributions of the detected γ-like clusters for both the normal and the modified events are shown in Fig. 21. It is seen that most of the extra γ–like clusters appear in the region where additional photons had been added. This also demonstrates that the PMD will be able to search for unusual events which may happen to change the distribution of particles within its acceptance.

4.4 Estimation of E_T^{em}

The PMD can be used to provide an estimate of the electromagnetic transverse energy E_T^{em} using the measured preshower signals. Although there are large fluctuations in the energy deposited by individual photons in a preshower detector, the fluctuation substantially reduces when the summed energies of a large number of particles are considered. For the preshower PMD, a working estimate of E_T^{em} can be given by the relation

$$E_T^{PMD} = \sum_i \Delta E_i . \sin \theta_i \tag{7}$$

where θ_i is the angle at which the i^{th} γ-like cluster appears, ΔE_i is the energy deposited in the sensitive volume of the PMD by the i^{th} cluster, and the sum runs over all the observed γ-like cluster. We denote E_T^{em} measured by the PMD as E_T^{PMD} to distinguish it from the calorimetric measurement of E_T^{em}.

The ratio of E_T^{PMD} to E_T^{em} is shown in Fig. 22. E_T^{PMD} is found to be a small (~ 2 %) but constant fraction of E_T^{em}. The ratio is constant with event–to–event fluctuations within 5%. Using calibration relation derived from the test beam results in the case of WA93 PMD to convert CCD pixel ADCs to MeV and the simulation results on the ratio E_T^{PMD}/E_T^{em}, the E_T^{em} derived from preshower measurements have been found to compare very well with the measurements of the same quantity using the MIRAC Calorimeter [32]. This should enable the PMD to provide the estimates of the global transverse electromagnetic energy. Very small fluctuation in the above ratio gives hope of using the E_T^{PMD} measurement to study event shapes and the global event characteristics e.g. energy density etc., in the same manner as is done by the calorimetric measurements.

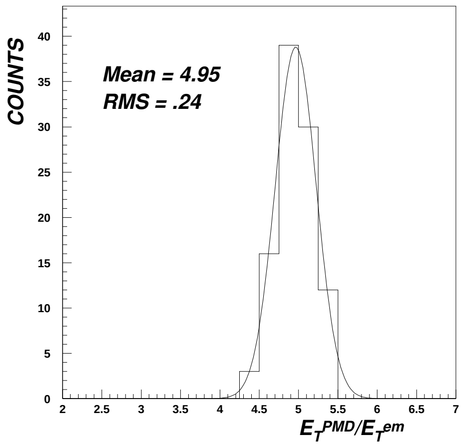

Figure 22: The ratio of E_T^{PMD} to E_T^{em} for the STAR PMD. The x-axis label is in arb. units.

4.5 Trigger Applications

The gas proportional counter design of the CPV with the proposed mixture of Ar + CO_2 + CF_4 is expected to provide very fast signals, as all the charge will be collected from the wires in less than 100 ns. This leads to a possible use of the CPV as a trigger detector as it will measure the multiplicity of charged particles in about 1.5 units of pseudo-rapidity in a region which will be complementary to the pseudo-rapidity range covered by the existing STAR trigger detectors CTB, TPC MWPC, VPD, VC and EMC (see Table 4E-2 of STAR CDR). Inclusion of CPV into the trigger system will increase the acceptance of the STAR trigger system to almost full range of pseudo-rapidity available at RHIC energy. Figure 23 shows the correlation between the number of pads hit in the CPV and the number of charged particles in minimum bias VENUS events in the actual environment of all detector subsystems. The nice straight line correlation despite low statistics clearly demonstrates the use of the CPV for trigger purposes and for tagging the impact parameter of collision.

By suitably instrumenting the electronics and implementing hardware-based algorithms, it is possible that trigger decision from the CPV is made available in less than 40 μs, which is the time for level-2 trigger. Such a scheme has been implemented in the preshower detector of the HADES experiment [38].

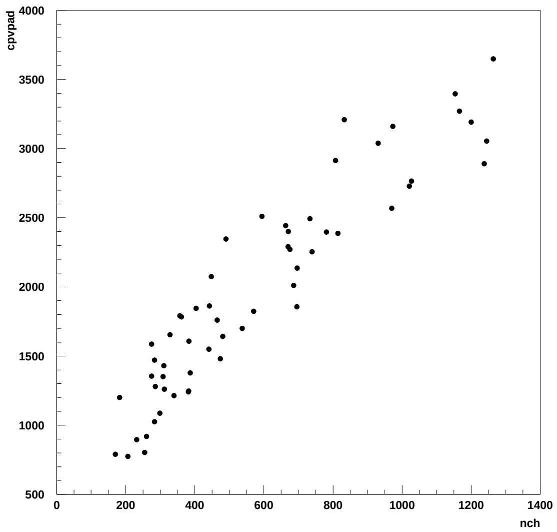

Figure 23: Correlation between the total number of pads hit in the CPV and the number of charged particles in minimum bias VENUS events.

5 R&D, Tests and Calibration

5.1 Preshower Detector

We plan to use the standard technology of the PMD based on the scintillator pads and WLS fibre light transport with II + CCD readout. This technology is well proven and hence no further R&D is required.

The testing of the newly fabricated PMD box modules with 12 mm pads will have to be carried out using the beams of electrons , muons and pions in the energy range 1–20 GeV. This will have to be carried out at any test beam facility at the BNL after the electronics and data acquisition are fully setup there. A set of calibration runs for the cameras will also form part of these tests.

5.2 Charged Particle Veto

The technology for the CPV will be new to us and lots of R&D are needed for this. We have already taken up the R&D of honeycomb cellular proportional chamber and one prototype was recently tested at CERN as described below.

5.2.1 Prototype Tests

A small prototype detector having 16×12 cells has been fabricated and tested at the secondary test beam facility of the CERN's Proton Synchrotron during September 1997. The detector shown schematically in Fig. 24 consists of a 9 mm thick G-10 gas–tight chamber with standard printed circuit boards on both faces. The inner volume is divided into 12 mm dia hexagonal cells by shaping thin (0.1 mm) copper foil. All the cell walls are internally connected and act as a common cathode. Gold plated tungsten anode wires of 20 micron dia. are stretched along the axis of each hexagonal cell with 35 gm tension and soldered on to the printed boards on both faces. The wires are divided into four groups of 48 channels and each group is connected to a 50 pin ERNI connector at the edge of the board as shown in Fig. 24. A mixture of 80% Ar and 20% CO_2 is used at atmospheric pressure and the chamber is operated in the proportional mode at 2 KV anode voltage. The front end electronics consists of 12 gassiplex chips readout by VME based C-RAMS modules as described in section 2.3.3.

The preliminary charge spectrum for 3 GeV π^- is shown is Fig. 25. In the present test the mean pedestal for gassiplex was 80 ± 20 channels which is rather high. Even then the MIP is well isolated.

The present test beam time was very short and essentially of parasitic nature. During this short test we gained valuable experience in handling the gassiplex electronics and C–RAMS based data acquisition. All the parameters could not be properly optimised and some problem was also encountered in controlling the composition of the gas mixture. Preliminary estimate of the efficiency for MIP detection is $\sim$ 70%. This low efficiency might arise due to fluctuations in the composition of the gas mixture and some leakage of air into the chamber. We hope to improve upon this by several modifications in the chamber design, test setup and more careful handling of the gassiplex electronics in future tests.

5.2.2 Further R&D and Tests

Several new features are proposed to be incorporated in the chamber for improved gas flow and gas tightness and extensive tests with radioactive sources and cosmic muons are planned in the coming months at Calcutta. The tests will be done in the actual environment of gassiplex electronics.

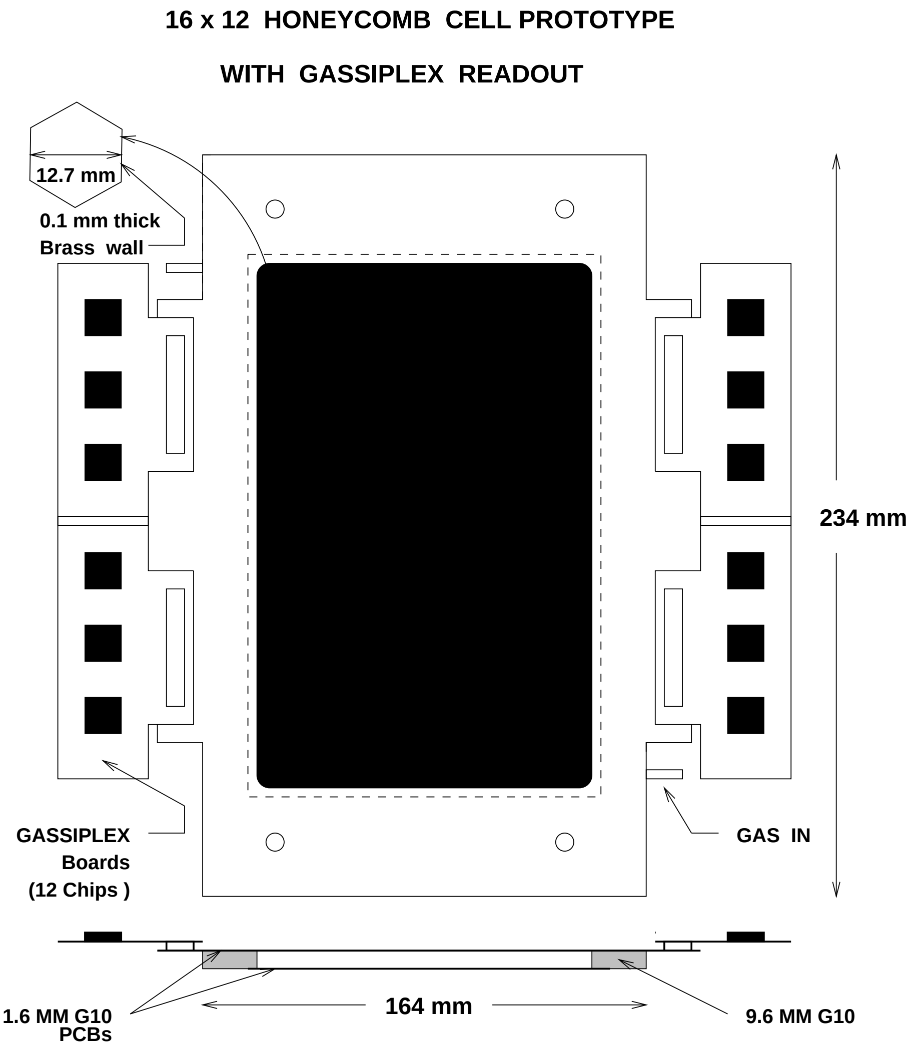

Figure 24: Schematic of the prototype gas cellular proportional chamber along with gassiplex board connections.

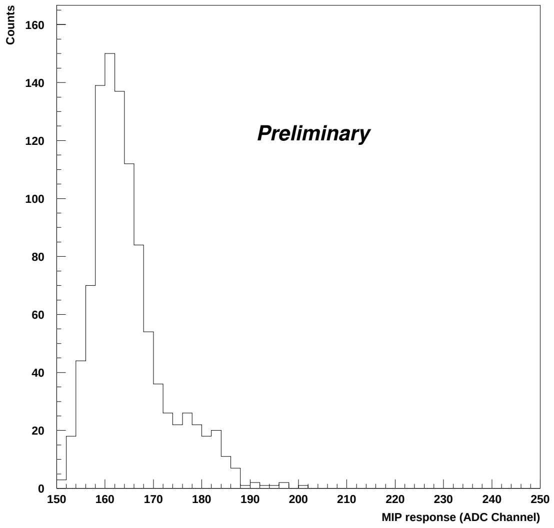

Figure 25: The total charge histograms for 3 GeV π^- obtained with the prototype cellular proportional chamber.

For the laboratory tests a test bench has already been assembled. Here the chamber can be sandwiched between two scintillator plates. The front paddle is a small scintillator finger with a 3×3×2 mm scintillator and can be positioned over any desired gas cell. The rear paddle covers the entire detector area. A collimated radioactive source in front can be moved to illuminate specific gas cells. The efficiency of any cell can be estimated by comparing the number of triple coincidences of the paddles and the cell to those of the coincidence between the paddles alone. The cell-to-cell gain variation can also be studied by positioning the collimated source and the finger scintillator over each cell. A reference proportional counter with a fixed radioactive source in the exit end of the gas flow line serves as a gain monitor and also checks the contamination in the gas, if any.

It is planned to have beam tests in 1998 at CERN during spring and autumn. We prefer to have beam tests at CERN because of the availability of experts on gassiplex electronics and also the C-RAMS based data acquisition system. CERN will be requested to provide the facilities.

Our attempt will be to perfect the cellular chamber as the baseline option as we have already developed a good understanding of this device. Recently there have been developments in GEM [39] and MICROMEGAS [40] type of gas chambers which also have good prospects. We are keeping close contact with these developments.

6 Engineering

6.1 Mechanical Integration

6.1.1 Installation and Servicing

The PMD will be mounted at z = 700 cm from the vertex on the side of the Wide Angle Hall. The horizontal and vertical dimensions are respectively 4 m and 3 m. The weight of the PMD will be approx. 3 tons. The depth the WA98 PMD is approx. 50 cm including the 6 mm thick iron support plate and the 17 mm thick lead converter plate. We want to hang a charged particle veto in front and this will take another 10 cm. The cables/connectors, gas lines for the CPV etc. will take another 10 cm. So a depth of 75 cm will be adequate for the PMD system. This space is presently available and has been earmarked for this detector [41] (Refer to the drawing no. SIM230–A–1).

Fig. 26 shows the schematic of the stand and the mechanism of fixing to the wall in the Wide Angle Hall. This needs firm grouting of four 3/4 inch thick steel anchor plates (size 10 inches x 6 inches), two on each side of the tunnel opening in the hall. Two 'I' beams with angled supports will be mounted on these plates (54 feet above the beam axis) and take the load of the PMD and the CPV. A 21 feet long, structurally reinforced beam moves across the 'I' beams parallel to the beam axis upto $\pm$ 30 cms from the 7 m position to facilitate service access and supports the transverse sliding movements of the two halves of the PMD. The hanging arrangement incorporates fine adjustments for level and skew of the detector planes for final alignment. The PMD has a vertical axis of symmetry and the two halves can be opened like a clam-saw. These two halves can be smoothly moved in the transverse direction along a horizontal support rail structure as shown in Fig. 26. Another light horizontal rail supports the two halves of the CPV in a similar fashion and shares the common side support beams. Thus the PMD and the CPV can be separately moved in and out without disturbing the alignment. During detector servicing the poletip support will have to be moved forward to make room for access.

A support structure for the vacuum pump located behind the proposed PMD site and the adjoining beam pipe support needs to be slightly modified to accomodate the PMD. A request for this has been communicated to the STAR engineers and very favourable response has been received.

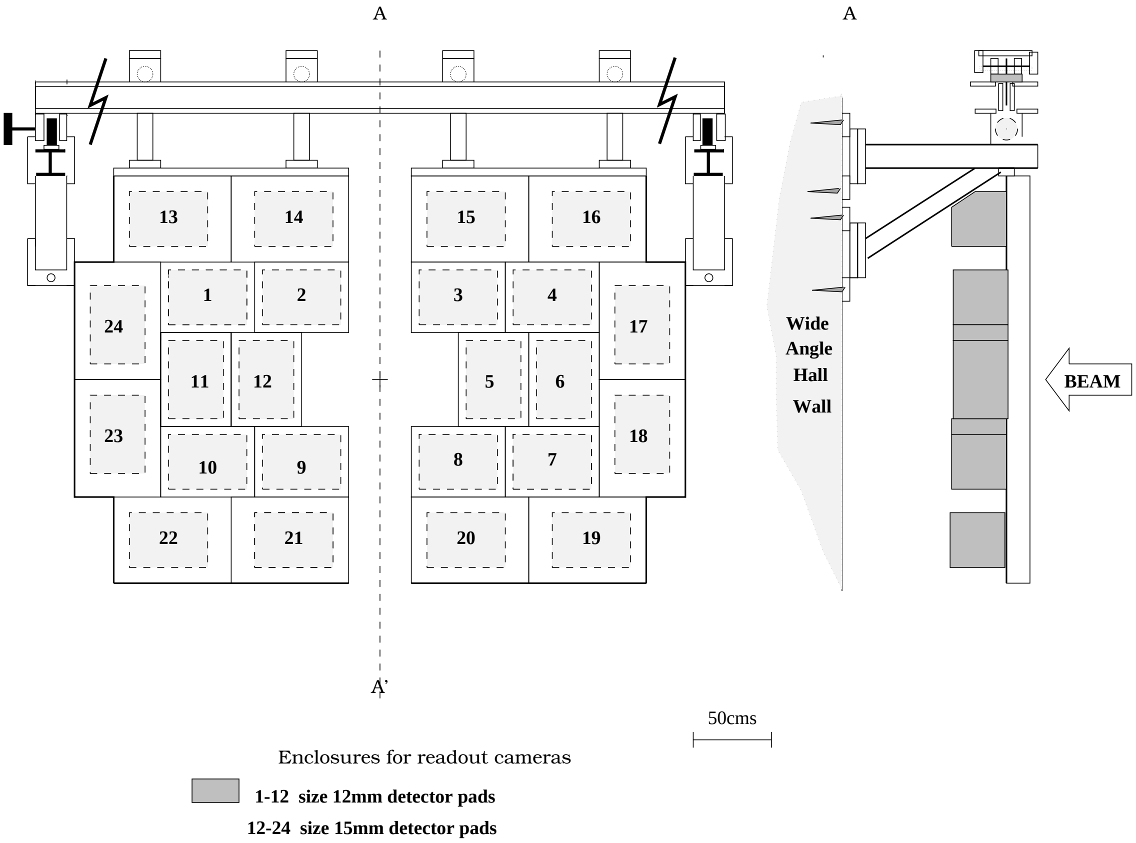

Figure 26: Schematic of the PMD stand.

6.1.2 Data Taking

The PMD being a photon detector requires little or no material in front. The major STAR components which come in the line of sight of the PMD are : the beam pipe, SVT, magnet poletip, FTPC and VPD. After several discussions with colleagues in STAR we have requested the following arrangements and received very favourable response [41, 42] :-

(i) The VPD will be placed inside the central hole of the PMD and will be supported by the PMD stand, The PMD has a vertical axis of symmetry and can be opened on the two sides like a clam-saw. Since the VPD also will have a similar design, it will be trivial to support the two halves of the VPD on the two halves of the PMD.

(ii) The poletip support will be kept fully retracted during data taking so that no big shadow is cast on the PMD. The layout shown in Fig. 26 makes the PMD vertically more compact. This will have much less interference from the poletip support in the fully retracted position.

6.2 Electrical Integration

The PMD requires five standard (six ft high, 19 inches wide) racks to house all the electronics. The racks need location close to the PMD final position (2-4 m away). Three of the racks need water cooling and house the fastbus crates for the digitizers, 3 eurocrates for CCD camera electronics, high voltage power supplies and the VME crates for C-RAMS. The other two non-cooled racks house 3 CCD low voltage power supplies (cooled by internal fans), a NIM crate for trigger electronics and high voltage distribution boxes (passive units).

Two new high voltage distribution boxes will be built to be fixed on two sides of the PMD halves. They move with the PMD and do not cause strain to the thick high voltage cables going to the PMD box modules. We already have all the cables of sufficient length to go to the various cameras (II + CCD systems of UA2) from the distribution box. The electronics is compact and most of the things will be brought from the WA98 experiment along with the fastbus digitizers, CCD electronics and HV supplies for the image intensifiers. The existing power supplies have provisions to change to 110V AC tap. Other units to be purchased new will have the electrical supply as per the US standards.

The estimated power requirement for the racks is **around 20 KVA** and should be provided at the site of the racks.

6.3 Integration of Trigger and Data Acquisition

6.3.1 Event Trigger and the CCD trigger

The relation between the main trigger from the event and the PMD data acquisition is shown by the timing diagram in Fig. 3 and is discussed in [25, 27]. The arrival of trigger generates clear veto and starts the readout of the CCD frames.

As in the WA93/WA98 experiments the PMD readout will depend on the arrival of trigger from the main trigger electronics. The electronics required to generate other logic pulses for the readout consists of a few standard NIM modules like gate and delay generator, coincidence units, fan-in/fan-out etc. and can be easily assembled.

6.3.2 Integration of Data Acquisition (DAQ)

The readout system of the PMD was obtained from UA2 experiment with all its hardware and software supports. UA2 readout was based on CAMAC-FASTBUS interface system. Main readout for CCD camera system was based on FASTBUS, which was modified for adoption in WA98 DAQ.

In WA98 we used 2 FASTBUS crates each containing 12 digitizers. Digitizers were custom-build modules having zero-suppression and data compaction facilities. Each crate contains an Aleph Event Builder (AEB), which is used as a Readout Processor for that crate.

In the digitizer, the CCD signal is amplified by a factor of 2 and digitised by an 8-bit FADC capable of sampling at a rate of 20 MHz with 5 MHz analog bandwidth. The FADC reference is set so that 1 ADC count corresponds to 1 mV at the output of the CCD. The digitisers also work as hardwired processors for the real-time data compaction. The digitizers contain in memory a map of which pixels to assign to each fiber. The total pulse height belonging to each fiber is summed and data are output for hit fibers. For normal data taking they perform the following sequence of operations :

(a) pedestal subtraction pixel by pixel,
(b) noise compensation, and
(c) pixel to fiber mapping.

The sequence is performed in a pipeline manner, so that no additional dead-time is introduced by the data processing. Total readout dead-time depends on the total data volume to be transported from the digitizers. With the reduction in data volume in digitizer hardware it is possible to reduce the readout dead-time considerably.

All the softwares necessary to run the digitizers and AEB's were obtained from the UA2 experiment. They were mostly written in Fortran language, which we could compile with RTF compiler in OS9 environment. As the basic data acquisition of WA98 was using the same environment, it was relatively easy to implement these softwares in WA98. Additional codes were written to integrate the PMD data in the main WA98 subevent and event builders.

The jobs being performed by the DAQ software are as follows :

AEB cpu receives an event interrupt from the sub-event builder cpu in VME through the interface board, connecting the VME subsystem Bus of the subevent builder with the AEB. The AEB polls the digitizer DONE flag, then starts a block transfer from the digitizer memory to the interface board memory. After completion of the block transfer the AEB informs the sub-event builder with a software interrupt, the sub-event builder then moves the data from the interface board into its own local memory for further transfer to the main event builder in the beam spill-off period. Pedestal measurements, digitizer tests and loading of pixel-to-fiber maps are performed locally by the AEB with the software provided by UA2 group.

After discussions with several DAQ experts of the STAR Collaboration [43], following changes have been found necessary in integrating the PMD DAQ into the main STAR DAQ.

(1) As there will be no copper connection between the detectors and the DAQ room, the present FASTBUS-VME copper interface using the AEB needs to be replaced with a fiber-optic interface. This also requires keeping all the electronics near the detector which should be feasible considering our WA98 experience. The fiber-optic interface however needs special attention.

One possible solution is to replace the AEB with a commercially available FASTBUS master module (STR340/SFI1) which has a built-in VME cpu. This module is a 2,3 or 4 FB slot wide FASTBUS master with embedded VMEbus (1,2 or 3 slots). A VME processor plugging into this VMEBus can execute FB cycles via a FB sequencer. It accepts one or two VME plug-in modules to open FASTBUS directly to fiber-optic channel. It supports all VME programming environments like LynxOS, Vxwordsm OS9. It also provides several software supports.

(2) With the replacement of FASTBUS master, software for the new master will have to be developed. From the experience of WA98 DAQ, this seems not to be a difficult problem. Following solutions are possible :

(a) As the new master supports OS9 environment, it should be possible to use the AEB codes with proper modifications using the libraries supplied with the module.

(b) It is also possible to convert all the existing Fortran and Assembly (only a few) codes into C languages to make it compatible to the STAR DAQ software usage.

Regarding the integration of PMD data into the main DAQ, we need help of the STAR DAQ personnel.

6.3.3 Event Rate and Pileup Handling

The interaction rate for Au + Au collisions at the presently stipulated highest luminosity will be about 1200/sec. It is foreseen that the luminosity will be increased in future by a factor of 10 so that the interaction rate will go up to 12000/sec. The Clear Clock of the CDD is generated every 10 μs and thus clears at the rate of 100 KHz. It is possible to increase this by a factor of two [27]. At this rate no substantial pileup of events is expected.

Pileup events, if any, can be easily inspected and filtered off–line by implementing a TDC. In the WA98 experiment, the time difference between the trigger and the last clear clock was recorded with a TDC having 10 μs range. The TDC spectrum is used offline to reject events, where clear clock appears very close, thereby clearing the event entirely or partially. This can also be implemented in the case of STAR PMD.

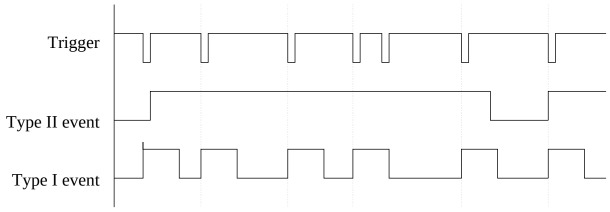

Figure 27: Timing logic for a two–level trigger for recording data of faster and slower detectors.

As the dead time of PMD readout is comparatively large ($\sim$ 10 ms), it may reduce the rate of data taking of faster detectors in the STAR setup. We therefore propose to use the following scheme as was used in the WA98 experiment.

Let us consider two detector systems having readout deadtimes of 1 ms (faster, referred to as Type I) and 10 ms (slower, referred to as Type II). The relation between the trigger and the two subevent deadtimes is shown in Fig. 27. When the Type II detector is busy, one can continue taking data for Type I. In the case illustrated here, one can take five Type I events, until Type II detector is ready to take data again. With this scheme the PMD will not cause any slowing down of data taking rate for the faster detectors.

7 Cost Estimates and Funding

Most of the equipment and the hardware will be available from the WA98 experiment. CERN has agreed to lend the UA2 cameras for use in the STAR experiment. The cost of extra detector box modules, charged particle veto, mechanics and electronics is given in Table V. The cost of the electronics for the charged particle veto is based on the latest data provided by J.C. Santiard of CERN.

TABLE V
Cost Estimates for the PMD and CPV

Item	Approx. Cost (USD)
WA98 PMD modification	
Scintillator and fibres	10,000
Fabrication and assembly	5,000
Power supplies	10,000
AEB Replacement CPU	10,000
Fastbus crate	30,000
CPV	
Gas counter	10,000
Gassiplex chips	80,000
PCBs and assembly	15,000
VME Crate	10,000
CRAMs/Sequencer	45,000
Mechanics and auxilliaries	15,000
TOTAL	240,000

It is expected that if the proposal is approved by the STAR Collaboration, it will be possible to seek funds from Indian sources. The STAR Collaboration is requested to provide the racks for electronics and the infrastructural support for cooling and electrical and mechanical integration of the PMD.

8 Timeline

A per chart showing timelines for various components of the job is given in Fig. 28. We aim to install the complete PMD and CPV subsystem in summer of 2000.

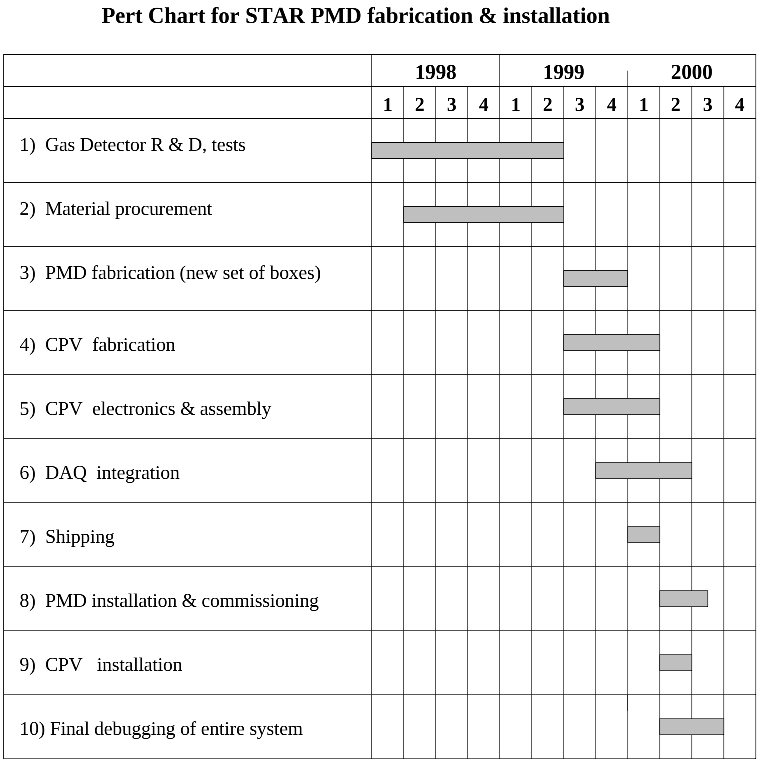

Figure 28: Pert chart of the PMD fabrication, installation and commissioning.

Based on our experience in fabricating the WA98 PMD, it is estimated that 12 detector box modules with 12 mm pads can be fabricated within six months. This job will be taken up in the later part of 1999. The gas counter design will be perfected during 1998 and the fabrication will start in early 1999. Electronic will also be procured and assembled in 1999. The detector stand will be shipped a few months before the expected arrival of the detector at site so that mechanical integration and familiarisation of the terrain is done well in advance.

Actual installation of the detector along with the electronics will take about three months time.

9 Acknowledgement

We are grateful to Hans Gutbrod for motivating us to seek further utilisation of the WA98 PMD at RHIC which resulted in our proposal to implement it in the STAR experiment. We are very grateful to R. Chidambaram and V.S. Ramamurthy for continuous encouragement and support in pursuing the physics of Quark-Gluon Plasma through international collaboration experiments. We have greatly benefited from many useful discussions with Burkhard Kolb of WA98 collaboration, J.C. Santiard of CERN and Rene Bellwied, Bill Christie, Hank Crawford, Volker Eckardt, Doug Fritz, Tim Hallman, John Harris, Huan Huang, Mike LeVine, Howard Matis and Peter Seyboth of STAR collaboration. Help of F. Piuz and A. Di Mauro during prototype tests at CERN is also gratefully acknowledged. We are grateful to L. Foa and CERN Management for permitting us to use the UA2 cameras for the STAR experiment. The financial support and encouragement by the STAR collaboration is also gratefully acknowledged. We thank Liz Mogavero for local arrangements during our stay at BNL in preparation for this proposal.

References

[1] J. D. Bjorken et al, "Baked Alaska",SLAC Preprint SLAC-PUB-6109 (1993); Proc. of Les Rencontres de Physique de la Vallee d'Aoste, ed. M.Greco, Editions Frontiers, p. 507 (1993).

[2] K. Rajagopal and F. Wilczek, Nucl. Phys. B399 (1993) 395.

[3] J.-P. Blaizot and A. Krzywcki, Phys. Rev. D46 (1992) 246.

[4] S. Gavin et al., Phys. Rev. Lett. 72 (1994) 2143.

[5] B. Muller, Rep. Prog. Phys. 58 (1995) 611.

[6] Krishna Rajagopal, Quark-Gluon Plasma 2, edited by R. Hwa, World Scientific, 1995.

[7] Krishna Rajagopal, e-Print Archive: hep-ph/9703258.

[8] Jorgen Randrup, Nucl. Phys. A616 (1997) 531.

[9] S. Pratt, Phys. Lett. B301 (1993) 159.

[10] C.M.G. Lates, Y. Fujimoto and S. Hasegawa, Phys. Rep. 65 (1980) 151.

[11] J. Lord and J. Iwai, International conference on HEP (Dallas, 1992); J. Iwai, (JACEE Collaboration) UWSEA 92-06.

[12] T.C. Brooks et. al. (Minimax Collaboration), Phys. Rev. D55 (1997) 5667.

[13] M.M. Aggarwal et al., WA98 Collaboration, submitted to Phys. Lett. B.

[14] T.K. Nayak et al., WA98 Collaboration, Proc. Int'l. Conf. on Physics and Astrophysics of Quark–Gluon Plasma (ICPAQGP'97), Jaipur (India) 1997; ed. B.C. Sinha, D.K. Srivastava and Y.P. Viyogi, Narosa Publishing House (in press).

[15] J. Bartke et al, ALICE Collaboration, Internal Note ALICE/PHYS 93-12.

[16] M. Gazdzicki and S. Mrowczynski, Z. Phys. C54 (1992) 127.

[17] M.M. Aggarwal et al, WA93 Collaboration, Phys. Lett. B403 (1997) 390.

[18] A.C. Das and Y.P. Viyogi, Phys. Lett. B380 (1996) 437.

[19] Tom Trainor, Proc. Int'l. Conf. on Physics and Astrophysics of Quark–Gluon Plasma (ICPAQGP'97), Jaipur (India) 1997; ed. B.C. Sinha, D.K. Srivastava and Y.P. Viyogi, Narosa Publishing House (in press).

[20] J. Cleymans, K. Redlich and D.K. Srivastava, 1997, e-print Archives nucl-th/9702004.

[21] R. Baur et al., CERES collaboration, Z. Phys. C71 (1996) 571.

[22] WA93 Collaboration, CERN/SPSC/90-14, SPSC/P252, May 1990.

[23] WA98 Collaboration, CERN/SPSLC/91-17, SPSC/P260, May 1991.

[24] M.M. Aggarwal et al, WA98 Collaboration, under preparation.

[25] M.M. Aggarwal et al, Nucl. Instr. Meth. in Phys. Res. A372 (1996) 143.

[26] M.M. Aggarwal et al, WA93 Collaboration, submitted to Phys. Rev. C (1997).

[27] R.E. Ansorge et al, Nucl. Instr. Meth. A265 (1988) 33; J. Aliti et al, Nucl. Instr. Meth. A279 (1989) 364.

[28] V. Balagura, Nucl. Instr. Meth. A368 (1995) 252.

[29] R. Vennhof, CERN Programme Library, entry W5050.

[30] P. Sarin et al., Proc. of Nucl. Phys. Sympo. (India) 1996.

[31] J.C. Santiard, private communication.

[32] S. Chattopadhyay, Thesis, Univ. of Calcutta 1996.

[33] V. Eckardt, Talk presented at the STAR Collaboration meeting at BNL during July 1997.

[34] Y. Takahasi et al., Nucl. Phys. A461 (1987) 263c.

[35] C. Peterson, T. Rognvaldsson and L. Lonnblad, LU TP 93-29; CERN-TH/7135–94.

[36] B.K. Nandi et al., WA98 Collaboration, Proc. Int'l. Conf. on Physics and Astrophysics of Quark–Gluon Plasma (ICPAQGP'97), Jaipur (India) 1997; ed. B.C. Sinha, D.K. Srivastava and Y.P. Viyogi, Narosa Publishing House (in press).

[37] Zheng Huang, Ina Sarcevic, Robert Thews, Xin-Nian Wang, Phys. Rev. D54 (1996) 750.

[38] B.W. Kolb, private communication.

[39] R. Bouclier et al., CERN–PPE/97-32, submitted to Nucl. Instr. and Meth. (1997).

[40] H. Gutbrod, private communications.

[41] H. Matis and D. Fritz, private communications.

[42] H. Crawford, private communications.

[43] M. LeVine, private communication.